J. Fluid Mech. (2005), *vol.* 531, *pp.* 293–324.
doi:10.1017/S0022112005004076 Printed in the United Kingdom

Vortex shedding from a hydrofoil at high Reynolds number

By DWAYNE A. BOURGOYNE, STEVEN L. CECCIO AND DAVID R. DOWLING

Department of Mechanical Engineering, University of Michigan, Ann Arbor, MI 48109, USA

(Received 6 June 2004 and in revised form 24 September 2004)

High Reynolds number (Re) wall-bounded turbulent flows occur in many hydro- and aerodynamic applications. However, the limited amount of high-Re experimental data has hampered the development and validation of scaling laws and modelling techniques applicable to such flows. This paper presents measurements of the turbulent flow near the trailing edge of a two-dimensional lifting surface at chord-based Reynolds numbers, Re_C, typical of heavy-lift aircraft wings and full-scale ship propellers. The experiments were conducted in the William B. Morgan Large Cavitation Channel at flow speeds from 0.50 to 18.3 m s^{-1} with a cambered hydrofoil having a 3.05 m span and a 2.13 m chord that generated 60 metric tons of lift at the highest flow speed, $Re_C \approx 50 \times 10^6$. Flow-field measurements concentrated on the foil's near wake and include results from trailing edges having terminating bevel angles of 44° and 56°. Although generic turbulent boundary layer and wake characteristics were found at any fixed Re_C in the trailing-edge region, the variable strength of near-wake vortex shedding caused the flow-field fluctuations to be Reynolds-number and trailing-edge-geometry dependent. In the current experiments, vortex-shedding strength peaked at $Re_C = 4 \times 10^6$ with the 56° bevel-angle trailing edge. A dimensionless scaling for this phenomenon constructed from the free-stream speed, the wake thickness, and an average suction-side shear-layer vorticity at the trailing edge collapses the vortex-shedding strength measurements for $1.4 \times 10^6 \leqslant Re_C \leqslant 50 \times 10^6$ from both trailing edges and from prior measurements on two-dimensional struts at $Re_C \sim 2 \times 10^6$ with asymmetrical trailing edges.

1. Introduction

High-Reynolds-number (Re) flows are commonly turbulent and the characteristics of the turbulence may depend on Re, particularly if the flow is wall-bounded. Here the disparate phenomena associated with near-wall viscous flow and nearly inviscid outer flow may compete with each other to cause subtle variations as Re increases. An example of mild Re variation at high Re is the gradual increase in the extent of the logarithmic portion of a boundary-layer velocity profile as the downstream-distance-based Re increases on a smooth flat plate. Another is the decline of the friction factor as the bulk-flow Re increases inside a smooth-walled pipe. When a wall-bounded flow separates, it carries its development history into the newly forming turbulent wake or shear layer and may thereby determine whether or not an organized pattern of vorticity (e.g. a vortex street) forms downstream of separation. Hence, Re-dependent features of the wall-bounded flow over an airfoil or hydrofoil can determine the relative strength of vortex shedding in the foil's wake. In applications of lifting surfaces,

vortex shedding is usually considered detrimental because it increases near-wake turbulence, structural vibration and hydro- or aeroacoustic noise.

This paper presents an experimental study of vortex shedding in the near wake of a two-dimensional hydrofoil at high Re and low Mach number. It documents how small geometrical changes of the trailing-edge apex angle and mild Re variations in the boundary layers that form on the hydrofoil govern the strength of near wake vortex shedding at chord-based Reynolds numbers, $Re_C = U_0 C/\nu$ (where U_0 is the flow speed far upstream of the foil, C is the chord length of the foil, and ν is the kinematic viscosity of the fluid) from near 1 million (1M) to more than 50 million (50M). These experiments span the Re-gap between prior airfoil and hydrofoil vortex-shedding studies (Re_C up to 2M or so), and commercial and military applications: heavy-lift aircraft wings and ship propellers ($30\text{M} \leqslant Re_C \leqslant 100\text{M}$). The results presented in this paper complement the average flow measurements reported in Bourgoyne *et al.* (2003).

Reduction, elimination, or control of vortex shedding has motivated research in this area for several decades. Blake (1986), and Blake & Gershfeld (1989) provide a comprehensive review of hydrofoil work through the mid-1980s. Their summary of experiments shows that trailing-edge vortex shedding may be pronounced on both symmetric and blunt trailing-edge geometries. Lotfy and Rockwell (1993) report on vortex shedding downstream of a blunt vibrating trailing edge and provide additional references to shedding studies. Prasad & Williamson (1997) review vortex dynamics pertaining to the wakes of bluff bodies based on the underlying instability of such flows. Huerre & Monkewitz (1990) and Oertel (1990) also provide overviews of flow instability and bluff-body wake flows, respectively. However, vortex-shedding results from bluff bodies are not readily transferred to streamlined bodies (struts and foils) because the greater distance between the leading and trailing edges of a streamlined body suppresses the interaction between near-wake flow fluctuations and leading-edge stagnation point motion compared to bluff-body flows. For the present purposes, a strut is a round-nose foil that is symmetric with flat parallel sides from its leading edge to approximately 80 % or 90 % chord with its final 10 % to 20 % possibly being asymmetric.

The aeroacoustics of lifting-surface vortex shedding has recently been studied both experimentally (Swales & Lowson 1997; Lurie, Reenan & Kerwin 1998; Minniti & Mueller 1998; Roger & Moreau 2002) and numerically (Ho & Lakshminarayana 1997; Knight & Peltier 1997; Howe 1999, 2000; Manoha, Traff & Sagaut 2000; Wang & Moin 2000, 2002). The most recent of these computational studies uses large-eddy simulations to predict the sound generated by a strut with a bevelled trailing edge (Blake 1975).

Similar aeroacoustic studies of vortex shedding and wake turbulence have also been conducted for compressor and turbine blades, and airfoil cascades. Bourgoyne *et al.* (2003) lists prior studies in this area that include both mean and fluctuating flow results. Cicatelli & Sieverding (1995) and Ubaldi *et al.* (1996) review studies of unsteady wakes from turbomachinery blades. More recent experimental work (Cicatelli & Sieverding 1996; Ubaldi & Zunino 2000; Rowe, Fry & Motallebi 2001) focuses on determining the frequency of vortex shedding.

The prior studies having the greatest significance for this one involve streamlined bodies at low Mach number. Greenway & Wood (1973) conducted an experimental study of vortex shedding behind two-dimensional struts with bevelled trailing edges at $Re_C \sim 1\text{M}$, and report that (i) vortex shedding can be altered with variations in the trailing-edge apex angle, and (ii) boundary-layer characteristics at the foil's trailing edge and their size relative to their vertical spacing are important factors for vortex shedding. They attribute this second observation to a number of prior investigations

including that of Gerrard (1966). Blake (1984) reports an investigation similar to that of Greenway & Wood (1973), but provides quantitative measurements of vortex shedding strength *via* wake velocity spectra. Sieverding & Heinemann (1990) observed that trailing-edge geometry and Re_C both affect the Strouhal number in the flow past a strut at low Mach number, and proposed that the state of the separated boundary layers determines the shedding process. These findings are replicated in the current study that also includes trailing-edge bevel angle changes, variable boundary-layer characteristics, and wake velocity spectra. In addition, Boldman, Brinich & Goldstein (1976) showed how unequal free-stream velocities on either side of a splitter plate could reduce vortex shedding from a blunt trailing edge. This result is relevant for the present study because the separated flow in the vicinity of the foil's trailing edge alters the Kutta condition, and unequal free-stream velocities may occur in the immediate vicinity of the foil's trailing edge.

The primary purpose of this paper is to report vortex-shedding results from an experimental study that extends prior findings to higher Re_C using a hydrofoil having two possible trailing-edge geometries and a non-trivial lift coefficient, $C_L \approx 0.52$ to 0.55 depending on Re_C and trailing-edge geometry (see Bourgoyne *et al.* 2003). Prior hydro- and aeroacoustic investigations were conducted at Re_C less than several million, well below the Re_C range of full-scale applications. In addition, much of the prior work has taken place on struts having lift coefficients well below that typical of hydrofoil and airfoil applications. Vortex shedding from a lifting surface may be different from that from a strut at the same Re_C with the same trailing-edge shape because the strut flow will not have the surface pressure gradients necessary for non-trivial lift. Surface pressure gradients influence the thickness of the boundary layers that develop on the foil and separate near its trailing edge, and these separated boundary layers interact to form the foil's near wake where a vortex street may form. A secondary purpose of this paper is to report the turbulence statistics measured in these unique high-Reynolds-number experiments, potentially to aid the development and validation of computational tools for high-Reynolds-number turbulence.

The remainder of this paper is divided into four sections. Section 2 covers the experimental set-up and techniques. Section 3 presents the flow-field measurements used to document how variation in Re_C or trailing-edge geometry may increase or decrease the prominence of trailing-edge vortex shedding. In § 4, a dimensionless scaling law, deduced from a cartoon of the near-wake flow, is used to collapse vortex-shedding strength measurements drawn from velocity spectra. The final section (§ 5) summarizes this work and states the conclusions drawn from it.

2. Experimental set-up and techniques

The test facility, test model, instrumentation, calibration and estimates of uncertainty in the mean flow measurements are described in Bourgoyne *et al.* (2003). This section provides a brief summary of that material along with additional experimental details relevant to the measurements of flow fluctuations near the trailing edge of the hydrofoil.

The hydrofoil was tested in the William B. Morgan Large Cavitation Channel (LCC), a low-turbulence recirculating water tunnel with a $3.05\,\mathrm{m} \times 3.05\,\mathrm{m} \times 13\,\mathrm{m}$ test section capable of steady flow speeds (U_0) from $0.25\,\mathrm{m\,s^{-1}}$ to $18.3\,\mathrm{m\,s^{-1}}$. The hydrofoil ($C = 2.134\,\mathrm{m}$ chord and 0.171 m maximum thickness, depicted in figure 1) was centred in and spanned the LCC test section for a 6 % blockage ratio. The suction side of the foil was the shape of a NACA-16 except for the trailing-edge bevel which had a 44°

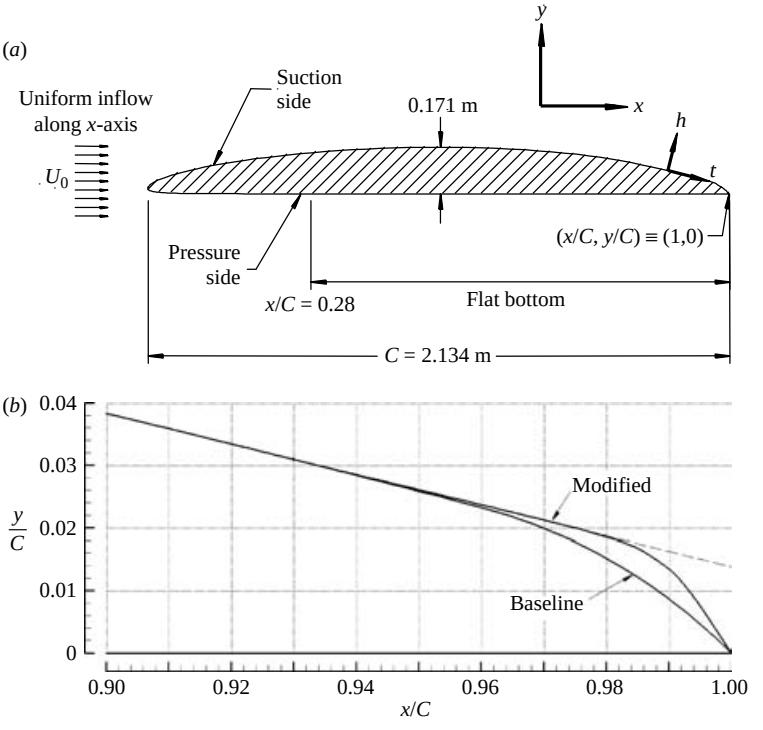

FIGURE 1. (*a*) The cross-section of the Geometry I hydrofoil with chord and max thickness indicated. The chord length given is the idealized value, measured to the vertex of the trailing-edge apex angle. This point is defined as $(x/C, y/C) = (1, 0)$ in the tunnel coordinate system: x-axis parallel to tunnel free stream, and y-axis vertical. Also depicted is the hydrofoil coordinate system, for which the t-axis is taken as the local surface tangent and the h-axis is the local surface normal. (*b*) Trailing-edge details showing Geometry I and Geometry II. The 0.4 mm radius, applied to the trailing-edge tip, is not depicted. The dashed line is tangent to the foil surface at $x/C = 0.930$.

(Geometry I) or 56° (Geometry II) apex angle. This type of suction-side trailing-edge bevel is a common geometrical feature of propeller blades that ensures structural integrity during severe off-design conditions, such as full reverse thrust. The pressure side of the hydrofoil was flat aft of 28 % chord. The foil's surface was polished to a nominal roughness of 0.25 μm, and neither the suction- nor pressure-side boundary layers were tripped. The foil's angle of attack (measured with respect to the flat portion of the foil's pressure side) for these tests was 0°. The foil generated 590 kN (60 metric tons) of lift at $U_0 = 18.3\,\mathrm{m\,s^{-1}}$. The LCC water temperature varied from 24 °C to 40 °C during these tests so the Re_C values quoted herein are for the average temperature of (32 °C) and have a nominal ±10 % variation.

Single-point two-component laser-Doppler velocimetry (LDV) and planar two-component particle-imaging velocimetry (PIV) were used to measure fluid velocity in the vicinity of the foil's trailing edge. Seed particles for the LDV and PIV systems were 2 μm nominal-diameter silicon carbide, and 16 μm silver-coated glass spheres, respectively. The LCC was flood seeded with both types of particles. The Dantec LDV system produced a long narrow focal volume (170 μm diameter, 6 mm length) oriented parallel to the foil span. The PIV system used two side-by-side LaVision Flowmaster 1024 × 1280 digital cameras, LaVision software, and two Spectra-Physics flash-lamp-pumped

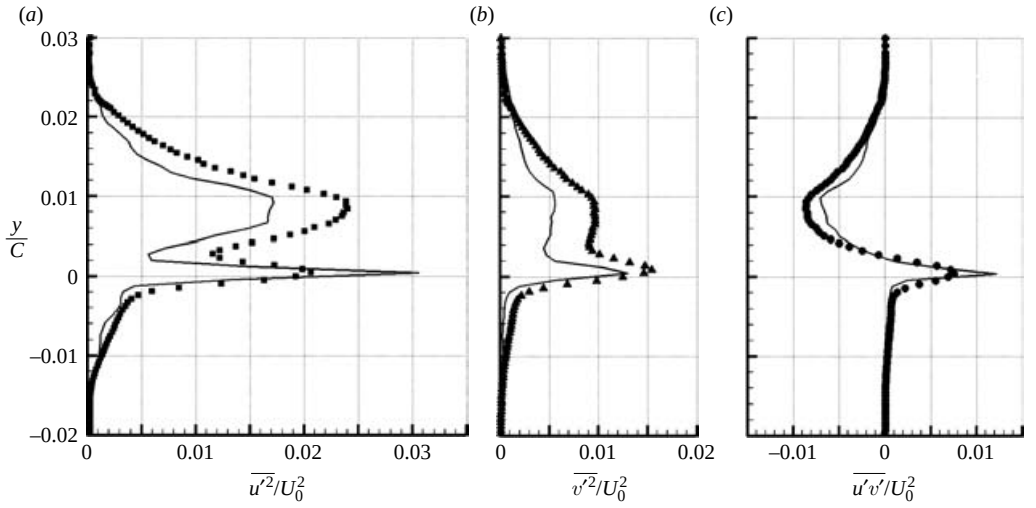

FIGURE 2. Comparison of velocity variances and Reynolds shear stress at $x/C = 1.0094$ with Geometry I at $Re_C = 50\text{M}$ between LDV (●) and PIV (——) measured results.

Nd-YAG lasers delivering 800 mJ per pulse at 532 nm. The PIV laser sheet thickness was 3 mm. The imaging ratio of 0.1 mm to 1 pixel and the 32 pixel × 32 pixel interrogation window – typically capturing ten particle pairs – set the PIV resolution at one fluid velocity vector for a cube 3 mm on a side. The image capture rate was ~1 Hz and 500 to 2000 images were acquired at each flow condition.

Uncertainties in the LDV-acquired and PIV-acquired velocity fluctuations include both bias and random errors. While bias error in the LDV velocity fluctuations is negligible, the fluctuations are presented as normalized quantities, so bias enters through the normalization value, U_0. This bias is estimated to be $\pm 0.2\,\%$ of the free-stream velocity. Random error in the LDV turbulence measurements was suppressed by averaging 500 to 12 000 particle bursts. Uncertainty in the instantaneous velocity vectors from the PIV is discussed in Bourgoyne *et al.* (2003). PIV-determined variances converged to within a few per cent after 2000 vector-field samples.

Although a direct comparison of LDV and PIV turbulence statistics showed differences in magnitude, both revealed similar trends and profile shapes. In general, the larger PIV sampling volume suppressed $\overline{u'^2}$, $\overline{v'^2}$ and $\overline{u'v'}$ compared to equivalent LDV measurements. Figure 2 shows the worst-case PIV–LDV comparison at $Re_C = 50\text{M}$ for the turbulence profiles recorded on a vertical line at $x/C = 1.0094$. Away from $y = 0$, the PIV turbulence levels were suppressed as expected by their greater spatial averaging compared to the LDV measurements. However, at $y \approx 0$, the PIV determined levels of $\overline{u'^2}$ and $\overline{u'v'}$ exceeded the LDV levels. At this location, the PIV interrogation volume includes fast-moving fluid that has passed close to the pressure side of the foil and slow-moving fluid in the suction-side separation bubble. A random distribution of particles in such an interrogation volume and the recursive PIV processing software, which attempts to discard spurious particle-pair correlations, tend to produce either the fast or slow velocity, as opposed to a spatial average, within the interrogation volume. Although this problem artificially raises the PIV-measured $\overline{u'^2}$ levels at this location, it appears to be confined to $1.00 < x/C \leqslant 1.01$ and $y \approx 0$.

In the present study, the two-component LDV was also used to acquire one-component temporal velocity spectra at fixed points in the foil's near wake. Dantec

U_0 (m s^{-1})	Re_C (million)	Symbol/line-type
0.5	1.4	– – – – ■ – – – –
1.5	4	——————▲——————
3.0	8	–·–·–·–·▼–·–·–·–
6.0	17	- - - - - -▶- - - - -
12.0	33	·····◀·····
18.3	50	– ·· –·· ●– ··–··

TABLE 1. Line and symbol types for flow speeds and Re_C values.

software (*BSA Flow*) was used to estimate the power spectrum from particle bursts having random arrival times. This software employs sample-hold re-sampling, Hanning windowing, and fast Fourier transform (FFT) spectrum calculations. The data re-sampling has the effect of a low-pass filter. No high-pass filtering was employed, but the maximum re-sampling frequency was maintained at two to three times the mean data rate as a compromise between frequency resolution and high-frequency aliasing. The reported spectra were truncated at the frequency above which aliasing may have occurred.

In addition to the fluid velocity measurements, dynamic surface pressure measurements were made with an array of flush-mounted pressure transducers (PCB 138M101) located at the PIV measuring plane and in the vicinity of the hydrofoil trailing edge. These sensors were arrayed in an 'L'-shape with lines of transducers set parallel and perpendicular to the flow direction. The results presented in this paper are from a single transducer located on the foil's pressure side nearest the trailing edge (x/C, y/C, z/S) = (0.990, 0, 0.36), where the x and y coordinates are defined in figure 1, z completes a right-handed set of Cartesian axes, and S is the foil's span. The time-resolved pressure signals were analogue band-pass filtered from 2 Hz to 5 kHz and sampled at 10 kHz. Temporal spectra were calculated from these measurements using approximately 3 million data points, partitioned with 50 % overlap to provide 376 spectral windows of 2^{14} (16 384) data points, with an estimated spectral amplitude uncertainty of ± 12 % (Vetterling, *et al.* 1992). A linear least-squares fit was subtracted from each partition to remove any drift and to zero the partition mean. Neither acceleration contamination nor background noise contributions were removed from these spectra, but a hundredth decade filter was applied to smooth the high-frequency portion of each spectrum.

Although the model and its mounting scheme were designed to be as rigid (and durable) as possible, some model vibration did occur. This was monitored with an array of eight accelerometers. A careful comparison of fluctuation spectra recorded by the trailing-edge pressure transducers and the nearest accelerometer(s) did not reveal any significant correlations in the frequency range of interest. Furthermore, when the measured acceleration fluctuations were converted to root-mean-square (r.m.s.) surface velocities, their normalized levels (0.01 %, worst case) were found to be well below that of the nominal peak free-stream turbulence level of the tunnel (0.5 %), and two or more orders of magnitude below the turbulent velocity fluctuations measured near the foil surface ($\sim$4 to 7%). Thus, the measurements reported here are believed to be free of model vibration contamination.

Experimental data were collected for both trailing-edge geometries at the flow speeds and Reynolds numbers given in table 1. This table also includes the symbols

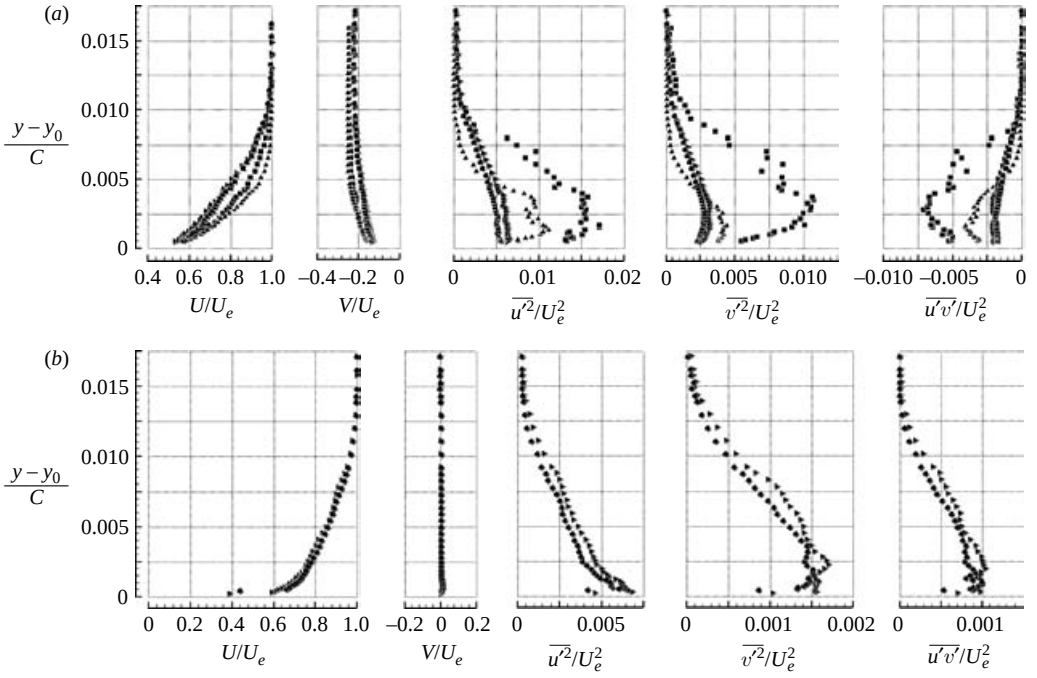

FIGURE 3. LDV-measured boundary-layer characteristics at $x/C = 0.93$ and $Re_C = 1.4$M, 4M, 17M, and 50M on the (*a*) suction-side and (*b*) pressure-side surfaces of the Geometry I hydrofoil. Panels show the normalized mean velocity components, velocity fluctuation variances, and Reynolds shear stress, all in the tunnel coordinate frame. Symbols are defined in table 1. No data are available at the lower two Re_C on the pressure side.

and line types used to designate results at the various Re_C values. Geometry I (44° trailing edge apex angle) and Geometry II (56° trailing edge apex angle) results are reported using filled and open symbols, respectively.

3. Results

The results are presented in two subsections. The first covers the measured turbulence statistics. The second documents the vortex-shedding characteristics of the hydrofoil.

3.1. *Turbulence statistics*

This presentation of results starts from the attached boundary layers and proceeds downstream. The intent is to provide enough information to facilitate numerical simulations of this flow. Here, the primary flow speed used for normalization of the turbulence statistics is the free-stream speed U_0. Although it is frame dependent, it provides a simple generic scale for the velocity differences that drive the turbulent separated and reverse flow near the foil's trailing edge.

LDV-measured characteristics of the attached boundary layers approaching the trailing edge ($x/C = 0.93$) are shown for the suction side (figure 3*a*) and pressure side (figure 3*b*) of the Geometry I hydrofoil at $Re_C = 1.4$M, 4M, 17M and 50M. Here, U and V are the x- and y-direction mean velocities, u' and v' are the x- and y-direction velocity fluctuations, y_0 represents the foil surface in figure 2(*a*), and U_e is the local horizontal flow speed at the outer edge of each boundary layer. These

profiles all represent turbulent boundary layers and the pressure-side measurements are consistent with flat-plate results (see Bourgoyne *et al.* 2003, § 3.4). The suction-side boundary layer has higher fluctuation levels at the lower two Re_C. The differences in the fluctuation levels are believed to originate in the differing lengths of laminar, transitional and turbulent boundary-layer flow on the suction side of the foil at each Re. Pressure-side boundary-layer measurements were not made for the lower two Re_C. The boundary-layer characteristics at $x/C = 0.93$ for Geometry II, although not measured, are presumed to be similar to those in figure 3.

Overviews of PIV-measured velocity fluctuation levels with Geometries I and II are provided in figures 4 and 5, respectively. The three panels show profiles of the normalized turbulent stresses, $\overline{u'^2}/U_0^2$, $\overline{v'^2}/U_0^2$ and $\overline{u'v'}/U_0^2$, at $Re_C = 1.4$M, 4M and 50M along with the foil's trailing edge. The grey vertical lines indicate the positions at which the profiles were measured. A relative scale for the levels is given at the lower left-hand side of each panel. The smoothly bending more-nearly-horizontal curves on each panel indicate the nominal vertical outer edges of the suction-side and pressure-side boundary layers and of the foil's wake, defined as the locations at which the streamwise velocity fluctuations fall to the noise level of the measurements. These nominal boundary-layer and wake-edge curves are plotted for $Re_C = 1.4$M, 4M, 17M and 50M in figures 4 and 5. Shadowing by the hydrofoil prevented PIV data acquisition on the foil's pressure side for $x/C < 1.002$.

The turbulence profiles shown in figures 4 and 5 are from the lowest (1.4M) and highest Re_C (50M) of this study, and from the intermediate Re_C (4M) with the strongest vortex shedding for both trailing edges. Results at the other Re_C have been omitted for graphical clarity. As Re_C increases, the profiles first tend from the 1.4M to the 4M results, and then from the 4M to the 50M results. The primary distinguishing feature of the profiles at $Re_C = 4$M is the large vertical velocity fluctuations found immediately downstream ($1.002 < x/C < 1.01$) of the Geometry II foil. In addition, the Geometry I profiles at $Re_C = 1.4$M are most dissimilar from the other Geometry I results. At this Re_C, the pressure-side boundary layer appears to separate upstream of the trailing edge (see § 3.4 of Bourgoyne *et al.* 2003), but was attached all the way to the trailing edge at every other Re_C investigated.

The Re and geometry-dependence of the near wake shown in figures 4(b) and 5(b) can be further illustrated by plotting the peak value of $\overline{v'^2}/U_0^2$ and its vertical location versus downstream distance. Such curves are given for $x/C > 1.005$ in figures 6 and 7 for Geometry I and II, respectively, at $Re_C = 1.4$M, 4M, 17M and 50M. In figure 6(a), the $Re_C = 1.4$M case is most different, and this is again attributed to pressure-side boundary-layer separation prior to the trailing edge. Results at the other Re_C are more similar, though close examination of figure 6(b) reveals some Re-variation in the downstream location of the maximum fluctuations. By comparison, dramatic Re-variation in the location of maximum fluctuations is shown for Geometry II in figure 7. Here, the point of maximum fluctuations resides near $x/C = 1.03$ at $Re_C = 1.4$M, progresses upstream towards the trailing edge as Re_C is increased to 4M, and then progresses downstream again when Re_C increases to 17M or higher. A comparison of figures 6(b) and 7(b) also shows that enhanced vertical velocity fluctuations occur with Geometry II.

Figures 8 and 9 follow the same format as figures 6 and 7, but give the downstream evolution of the normalized Reynolds shear stress, $-\overline{u'v'}/U_0^2$, for $Re_C = 1.4$M, 4M and 50M. The $Re_C = 17$M results lie very close to those at 50M and have been omitted for graphical clarity. The shear stress profiles have two extremes of opposite signs, and the coordinates and values of both are plotted. In figures 8(a) and 9(a), the vertical

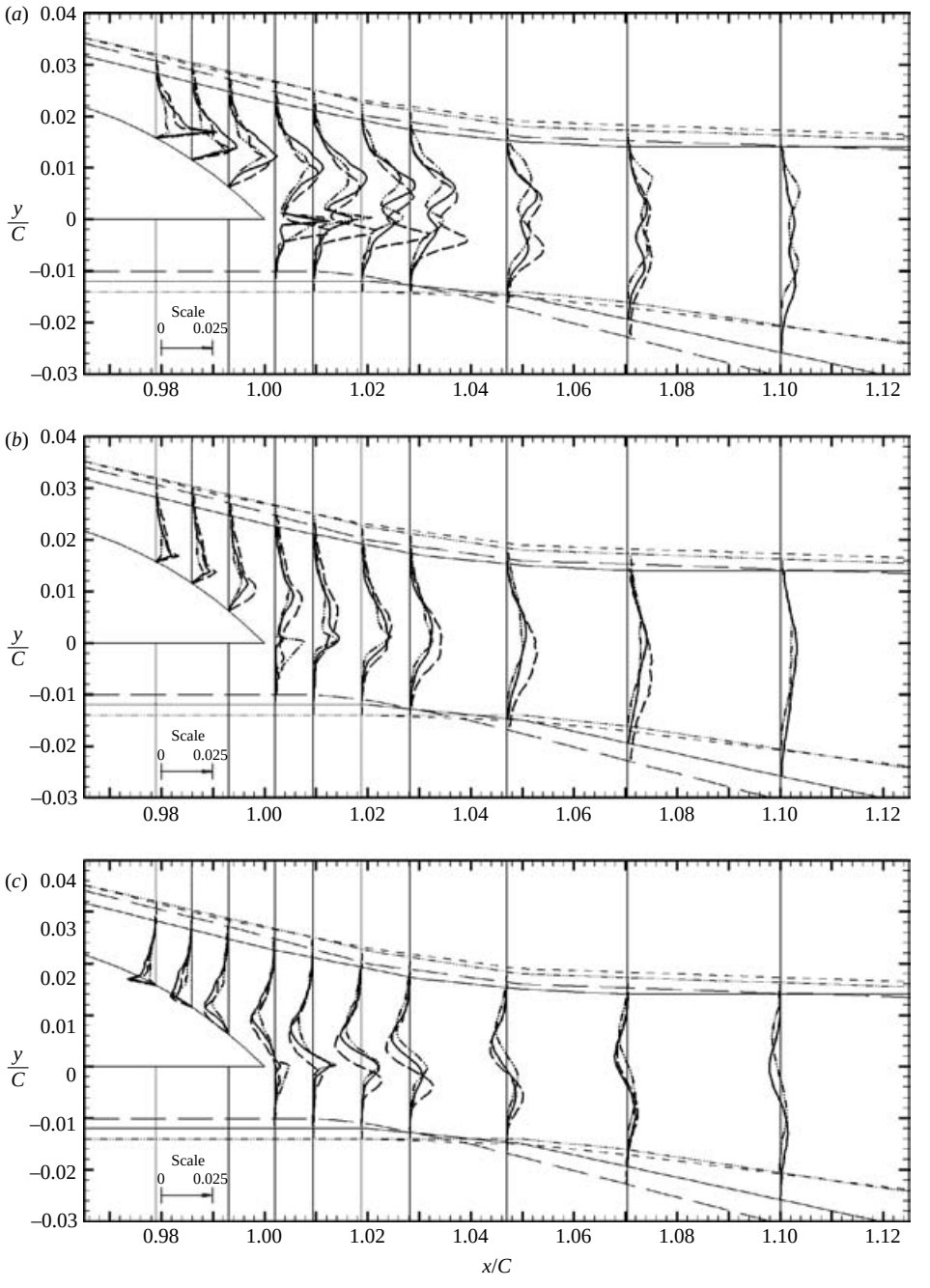

FIGURE 4. PIV-measured separating boundary layer and near-wake fluctuations for Geometry I at $Re_C = 1.4$M, 4M and 50M presented as normalized (*a*) streamwise fluctuations $\overline{u'^2}/U_0^2$, (*b*) vertical fluctuations $\overline{v'^2}/U_0^2$, and (*c*) Reynolds shear stress, $\overline{u'v'}/U_0^2$. The trailing-edge geometry is depicted in the left-hand half of each frame. Vertical grey lines are shown at the x/C coordinate of the measurements and provide the vertical axis for the plotted profile. The scale used to set the horizontal extent of each profile is provided in the bottom left-hand corner of the frame. The smooth nearly horizontal curves mark the outer edges of the suction-side and pressure-side boundary layers and of the foil's wake. Data are presented at $x/C = 1.002$ in lieu of $x/C = 1.000$. Line types are defined in table 1. Data at $Re_C = 1.4$M were not available at the downstream station.

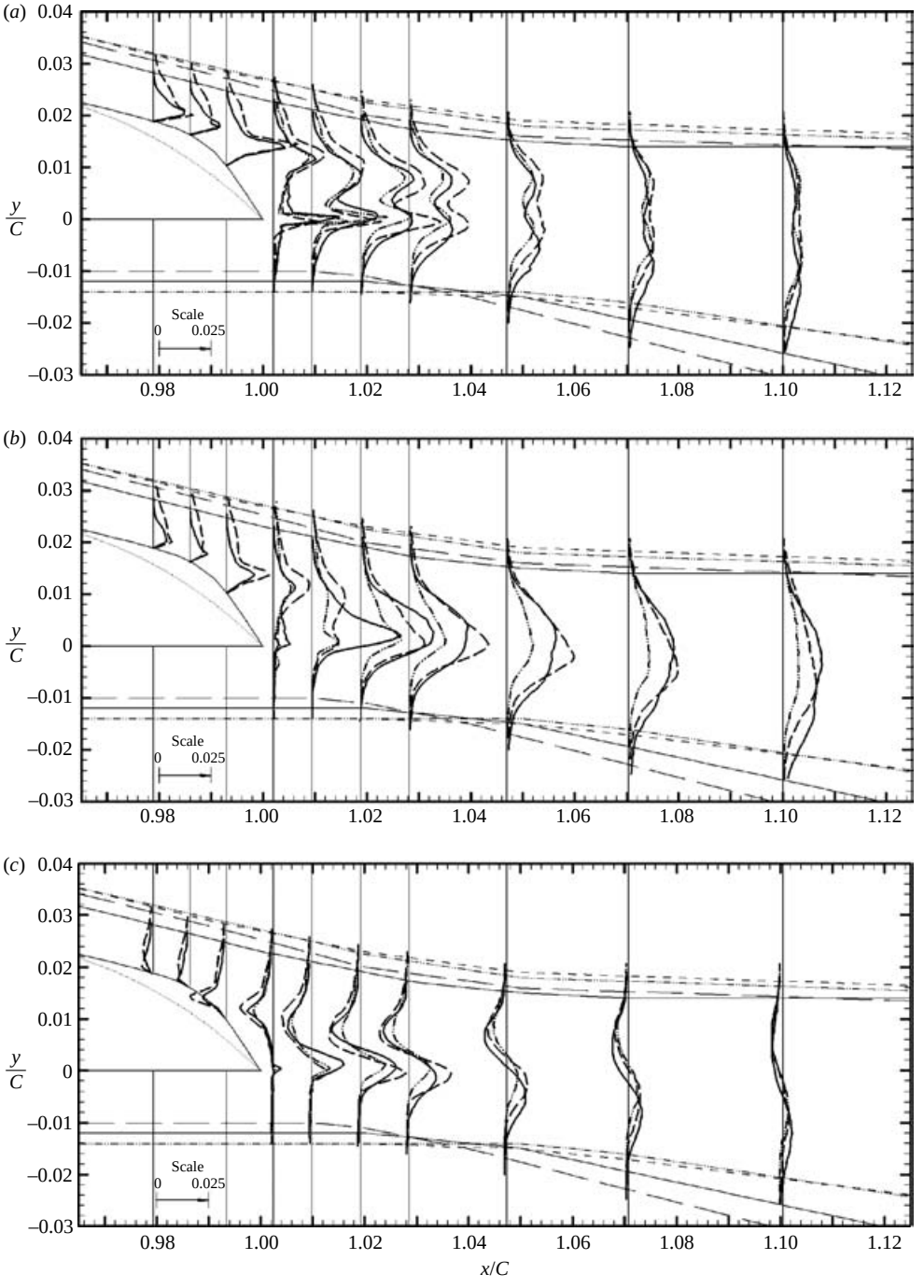

FIGURE 5. PIV-measured separating boundary layer and near-wake fluctuations for Geometry II $Re_C = 1.4$M, 4M and 50M, presented in the format of figure 4. Data at $Re_C = 50$M was not available at the three upstream stations.

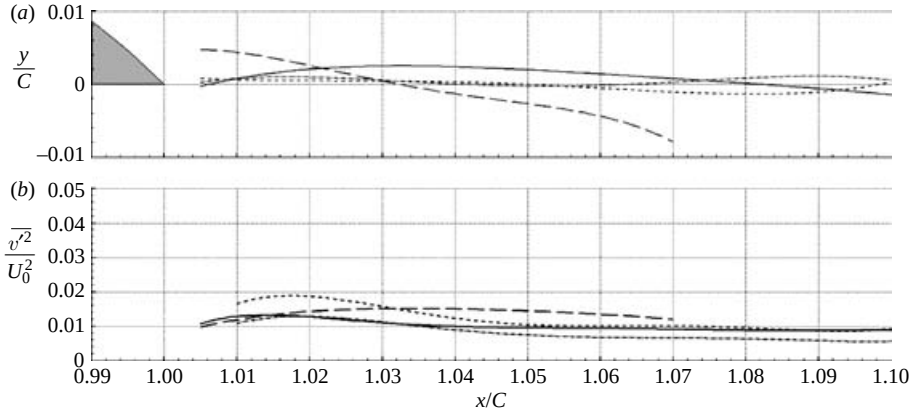

FIGURE 6. Loci of maximum vertical velocity variance at $Re_C = 1.4$M, 4M, 17M (*a*) and 50M, taken from figure 4 for Geometry I, and (*b*) vertical velocity variance values at these loci.

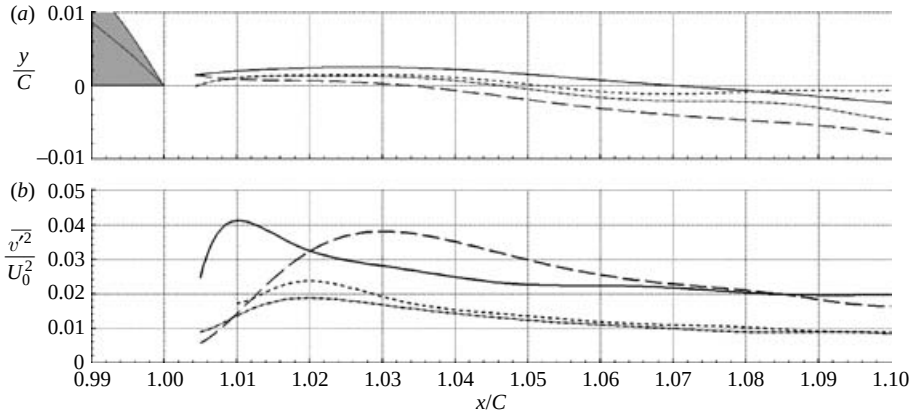

FIGURE 7. Same as figure 6 except these data are for Geometry II.

distance between curves for the same Re_C indicates the near-wake thickness. Although the various curves for each Re_C are different, in all cases, the near-wake thickness decreases, reaches a minimum, and then increases with increasing downstream distance; and the minimum wake thickness coincides with the downstream location of the Reynolds shear stress extremes. This flow behaviour is consistent with prior investigations (see Blake 1986). However, the distance from the trailing edge to the location of the peak in Reynolds stress varies with Re_C, and like the $\overline{v'^2}/U_0^2$ results, a comparison of peak $\overline{u'v'}/U_0^2$ levels in figures 8(*b*) and 9(*b*) shows enhanced shear stress occurs in the pressure-side shear layer with Geometry II. Higher turbulence levels occurring nearer the trailing edge indicate vortex shedding in this flow.

To complete the presentation of turbulence statistics, figures 10, 11 and 12 show the near-wake evolution of plane-wake-normalized vertical profiles of $\overline{u'^2}$, $\overline{v'^2}$ and $\overline{u'v'}$, respectively, at $x/C = 1.002$, 1.009, 1.028 and 1.047 for $Re_C = 1.4$M, 4M, 17M and 50M. The horizontal axes on figures 10 to 12 are normalized by ΔU_{max} where $\Delta U = U(y) - U_e^{ss}$ (U_e^{ss} is the suction-side wake-exterior horizontal velocity). The vertical axes on these figures are $(y - y_{ctr})/y_{1/2}$. Here, y_{ctr} denotes the average of the vertical coordinates where $\Delta U = \Delta U_{max}/2$. The values for y_{ctr}, ΔU_{max}, and $y_{1/2}$ are provided

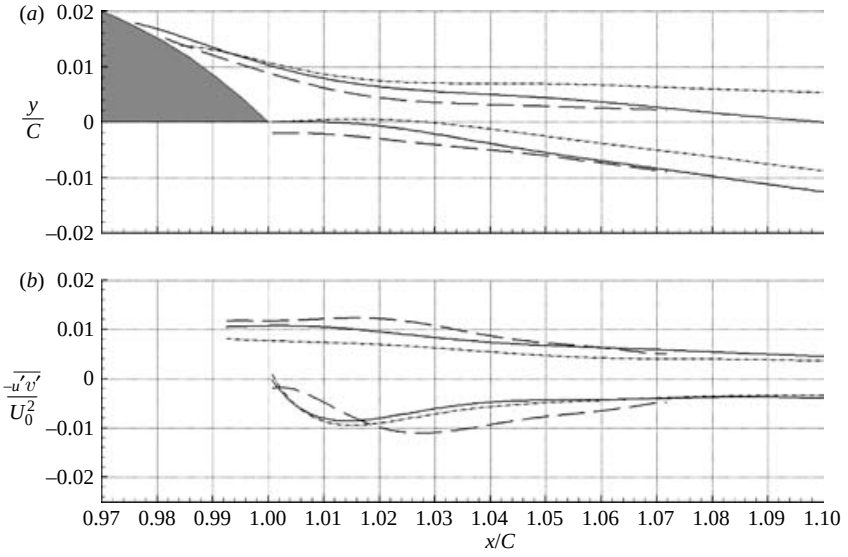

FIGURE 8. Same as figure 7 except these data are for the normalized Reynolds shear stress. Data at $Re_C = 17$M are omitted for clarity, but are similar to $Re_C = 50$M.

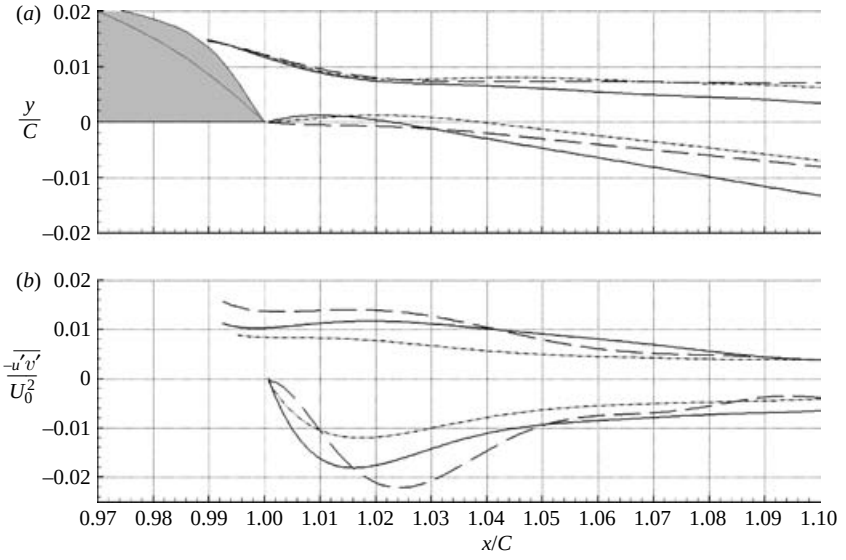

FIGURE 9. Same as figure 8 except these data are for Geometry II.

in Bourgoyne *et al.* (2003). For comparison, profiles for the self-similar wake of a symmetric airfoil at $Re_C \sim 10^4$ (Wygnanski, Champagne & Marasli 1986) are plotted on the right-most frames of figures 10 and 12.

The plane wake coordinates are effective in collapsing the turbulence profiles for both trailing-edge geometries at $x/C = 1.002$ except for $\overline{u'^2}$ at $Re_C = 4$M (figure 10*b*). However, as the wakes evolve downstream, profile differences between the two trailing-edge geometries increase, particularly at the lower two Re_C. Most striking is $Re_C = 4$M,

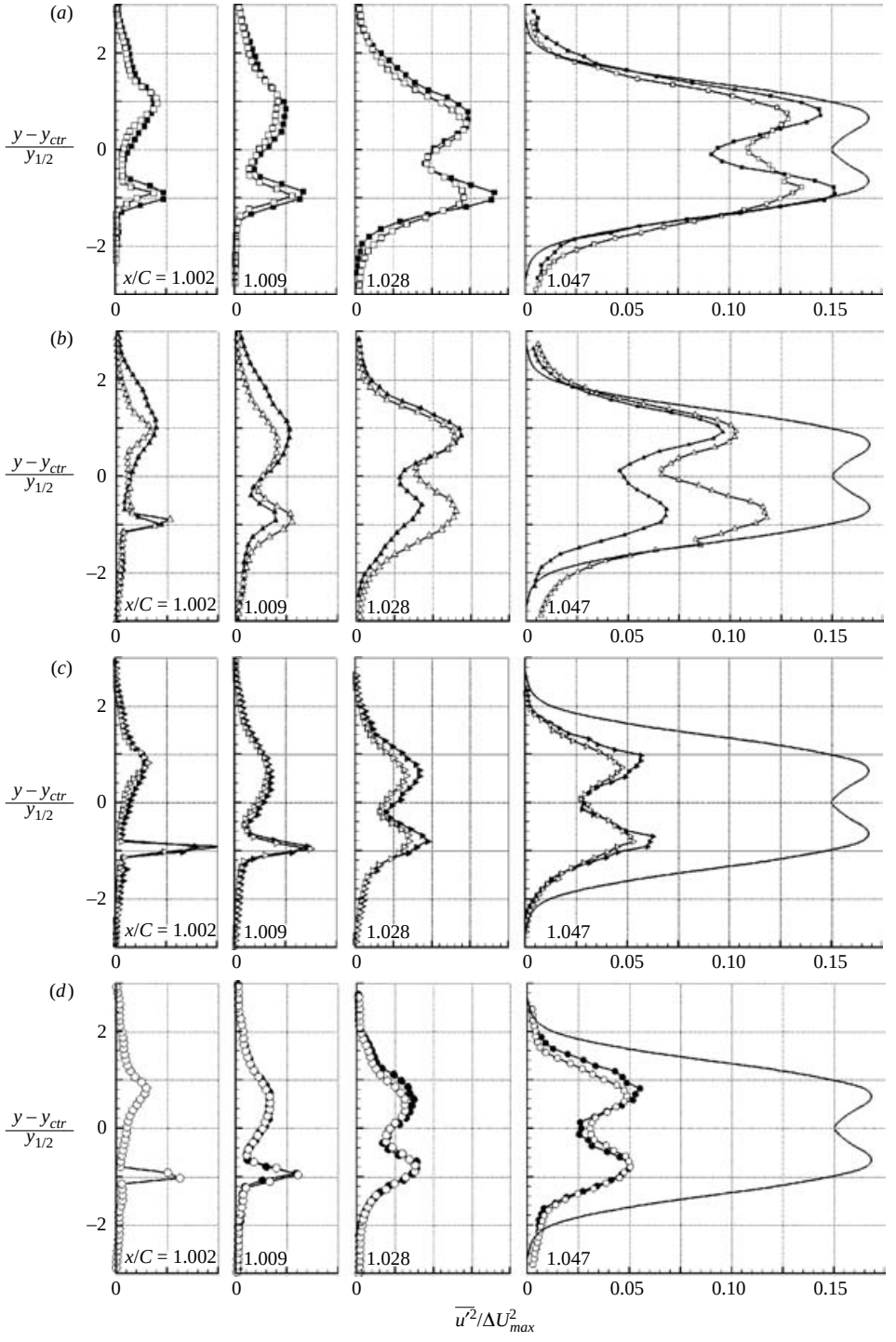

FIGURE 10. PIV-measured streamwise velocity variance in the near wake for Geometry I (filled, symbols) and Geometry II (open symbols) at varying x/C for (*a*) $Re_C = 1.4$M, (*b*) 4M, (*c*) 17M, (*d*) 50M. The data are plotted in wake coordinates and scaled by the time-averaged velocity deficit, ΔU_{max}. The x/C coordinate is indicated in each panel. The solid line in the far right-hand panel gives the self-preserving wake profile of a symmetric airfoil at $Re_C \sim 10^4$ (Wygnanski *et al.* 1986).

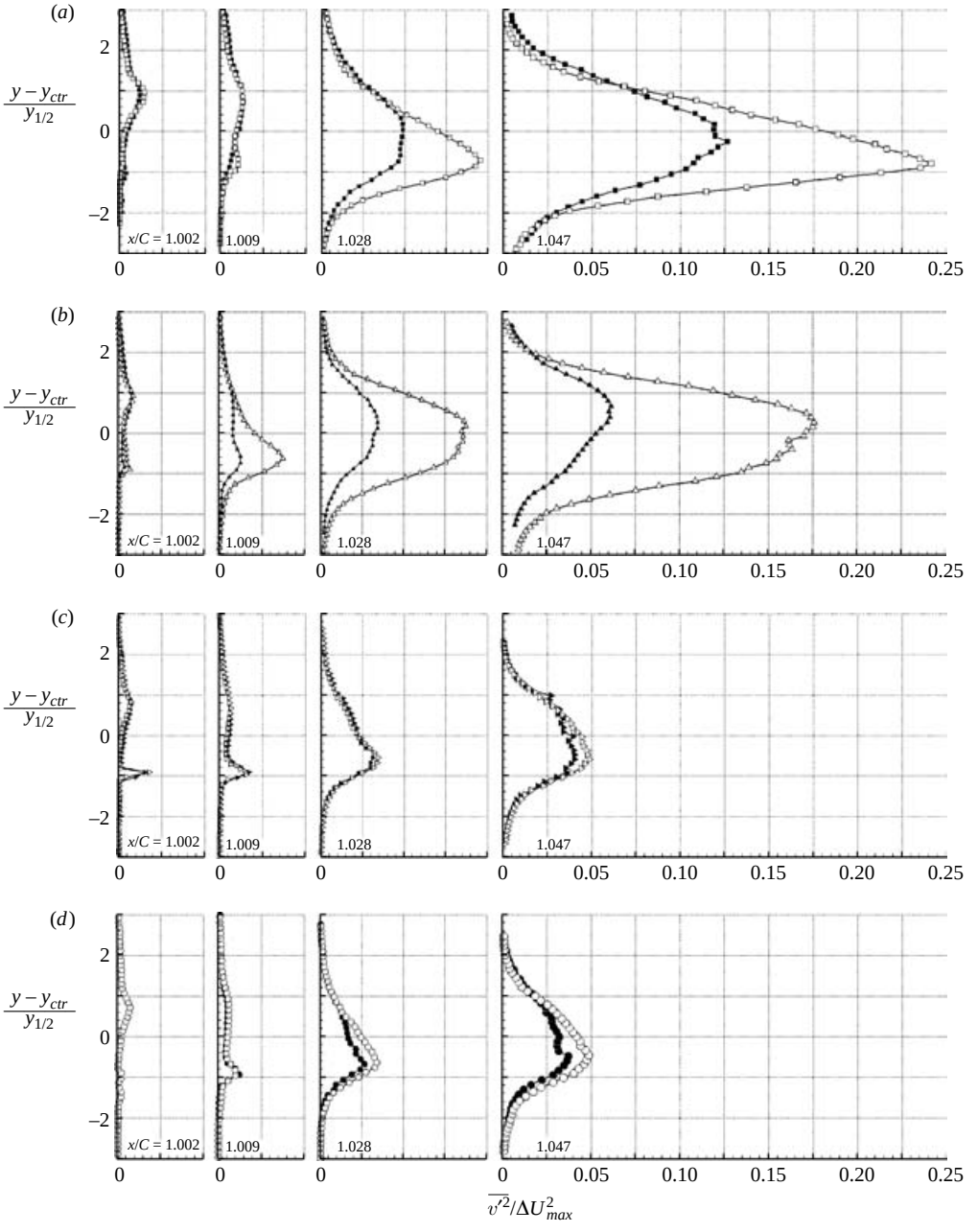

FIGURE 11. Same as figure 13 except these data are for the normalized vertical velocity variance.

for which the fluctuations associated with the pressure-side shear layer grow more rapidly for Geometry II than for Geometry I. The presence of stronger vortex shedding with Geometry II is the primary physical difference in the two flows at this Re_C. Similarly, at $x/C = 1.047$, the wake-normalized turbulence levels decrease by more than a factor of two as Re_C increases from 1.4M to 50M (compare the right-hand panels of parts (*a*) to (*d*) in figures 10–12). While some of this variation arises

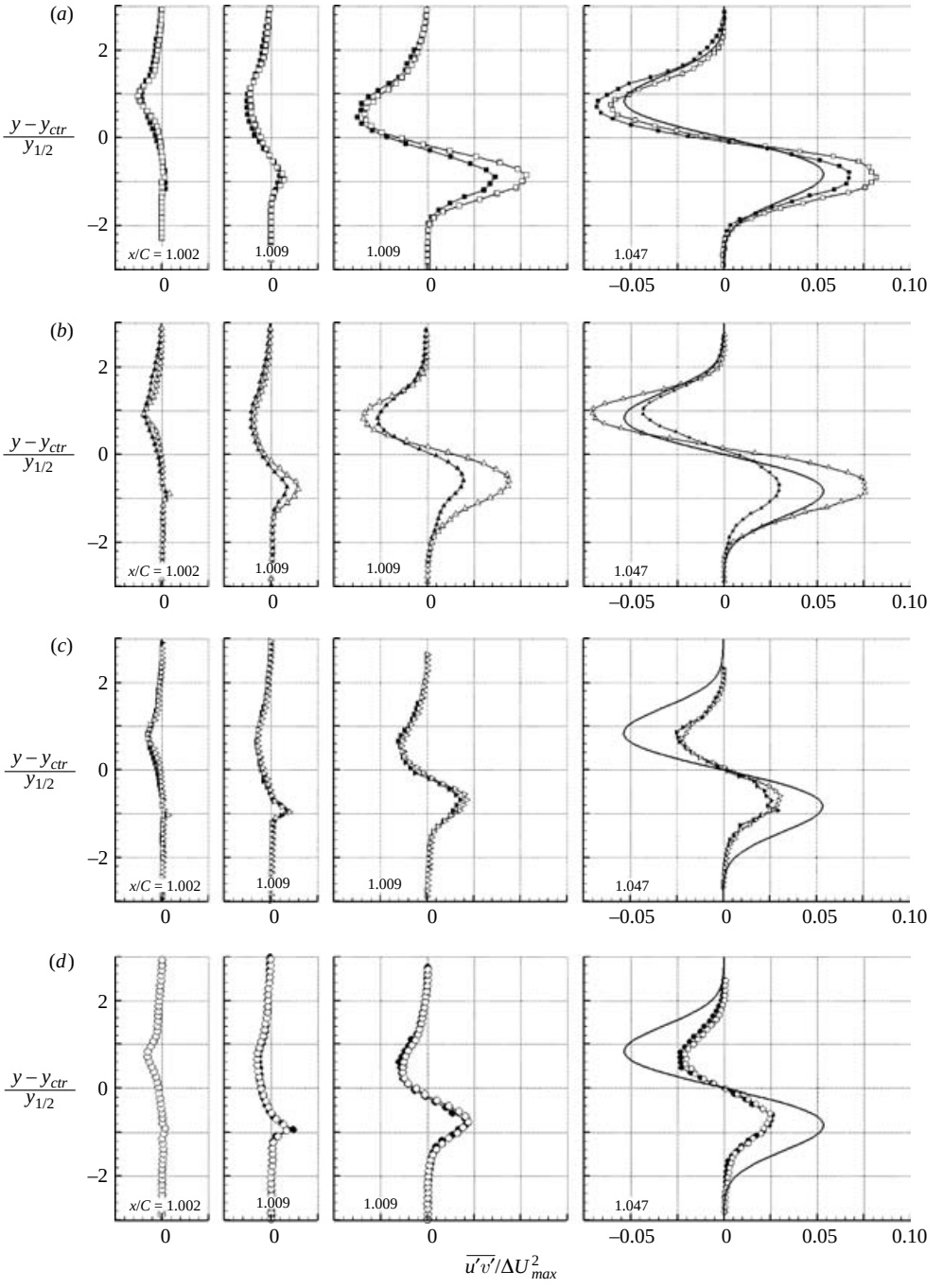

FIGURE 12. Same as figure 13 except these data are for the normalized Reynolds shear stress.

from the fixed PIV spatial resolution, the remainder appears to be a genuine *Re*-effect associated with the relative strength of vortex shedding (see § 3.2). In addition, the results at the lowest Re_C of this study (1.4M) are the best match with the prior foil wake measurements at $Re_C \sim 10^4$.

Re_C (million)	$x/C = 1.0094$		$x/C = 1.0703$	
	Geometry I	Geometry II	Geometry I	Geometry II
1.4	0	0.0023	−0.0046	−0.0094
2	0	0.0023	−0.0023	−0.0046
3	0.0023	0.0023	−0.0023	−0.0023
4	0.0023	0.0023	0	−0.0023
8	0.0023	0.0023	0	0
17	0.0023	0.0023	0	0
50	0.0023	0.0023	0	0

TABLE 2. y/C Spectral measurement locations of the LDV focal volume.

3.2. *Vortex shedding*

To understand better the turbulence profile variations observed at different Re_C and with different trailing-edge geometries, temporal spectra were measured in the foil's near wake and an analysis of the spatial distribution of resolved vortices was undertaken.

Vertical velocity fluctuation spectra, $\boldsymbol{\Phi}_v(f)$, were measured in the foil's near wake at $x/C = 1.01$ and 1.07. The y-coordinate for each spectral measurement was chosen by searching for the maximum spectra peak height within the range $-0.025 < y/C < +0.025$ at the given x/C location. Typical results at $Re_C = 1.4$M, 4M, 17M and 50M are shown for Geometries I and II in figure 13. Only spectral values below the effective Nyquist frequency set by the LDV data rate are plotted. In addition, the data from $Re_C = 50$M were smoothed for graphical clarity. In all cases, the maximum spectral peak height and maximum spectral peak area were found in the immediate proximity of the pressure-side shear layer. Lesser spectral peaks were typically associated with the suction-side shear layer. The coordinates of the spectral peaks at $x/C = 1.01$ and 1.07 are provided in table 2 and are nearly coincident with the loci of maximum $\overline{v'^2}/U_0^2$ shown in figures 6 and 7. The temporal spectra shown in figure 13 were normalized so that $\overline{v'^2}/U_0^2 \equiv (\Delta_y^{nom}/U_0)\int_{-\infty}^{+\infty} \tilde{\boldsymbol{\Phi}}_v \, \mathrm{d}f$, where $\Delta_y^{nom} = 0.01C$ is a constant nominal wake thickness, $\tilde{\boldsymbol{\Phi}}_v(f)$ is the normalized spectra, and f is the temporal frequency in Hz. Reference lines with a slope of $-5/3$ are provided on both parts of figure 13.

The various vertical velocity spectra all have several common features. For $f\Delta_y^{nom}/U_0$ less than ~ 0.1, spectral levels are flat as f decreases, and for $f\Delta_y^{nom}/U_0$ greater than ~ 0.5, the expected spectral power-law for high-Reynolds-number turbulent fluctuations is recovered. In between, every spectrum displays a peak – to a greater or lesser degree – that indicates the strength of vortex shedding. These spectral peaks occur at different normalized frequencies, with differing heights and widths, but always near the anticipated Strouhal number, St, for near-wake vortex shedding from foils and struts (Blake 1986): $St = f_p\Delta_y/U_0 \approx 1/2\pi$. Most notably, Geometry II produces higher spectral peaks than Geometry I at every Re_C, with the highest spectral peaks occurring at $Re_C = 4$M for both trailing-edge geometries.

Vortex-shedding spectral-peak results for all seven Re_C of this study are presented in figures 14 and 15 for $x/C = 1.01$ and 1.07, respectively, using the parameters schematically defined in figure 16. Figures 14(e) and 15(e) give the frequency of the spectral peak, f_p, in the dimensionless form $2\pi St = 2\pi f_p\Delta_y^{nom}/U_0$. The Re_C and geometry dependencies noted above are further evident in figures 14 and 15. The spectral peak for $Re_C = 4$M with Geometry II has the greatest magnitude and the minimum

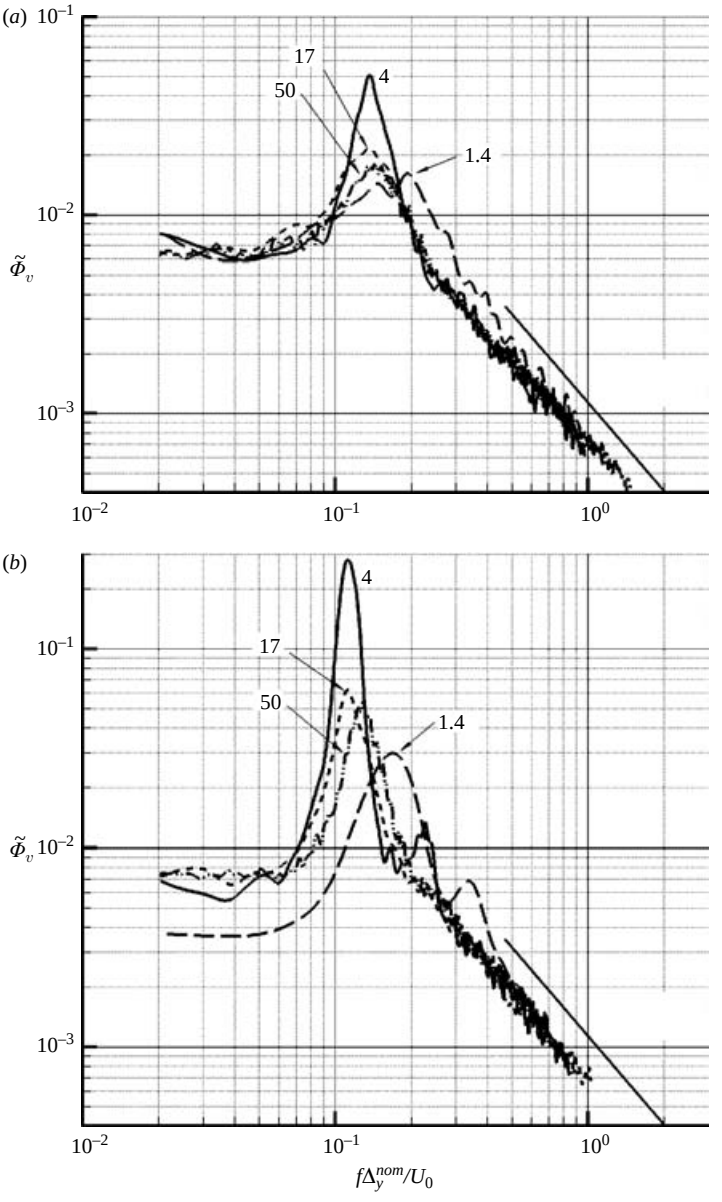

FIGURE 13. Near-wake LDV-measured temporal power spectra of vertical velocity fluctuations at $x/C = 1.07$ at $Re_C = 1.4$M, 4M, 17M and 50M for (*a*) Geometry I and (*b*) Geometry I. These data were taken at the location of peak vertical velocity fluctuations; table 2 gives their y/C locations. Numerals indicate Re_C in millions. The line to the right of the data has a slope of $-5/3$.

width. Comparison of figures 14 and 15 also reveals that the normalized spectral peaks are lower at $x/C = 1.07$ when compared to those at $x/C = 1.01$. However, the spectral energy ratio, $(\tilde{\boldsymbol{\Phi}}_v^{peak} - \tilde{\boldsymbol{\Phi}}_v^{base})\Delta\tilde{f}(\overline{v'^2}/U_0^2)$, actually increases from $x/C = 1.01$ to 1.07, and this indicates that a greater fraction of the vertical velocity fluctuations occurs at the shedding frequency as the flow evolves downstream.

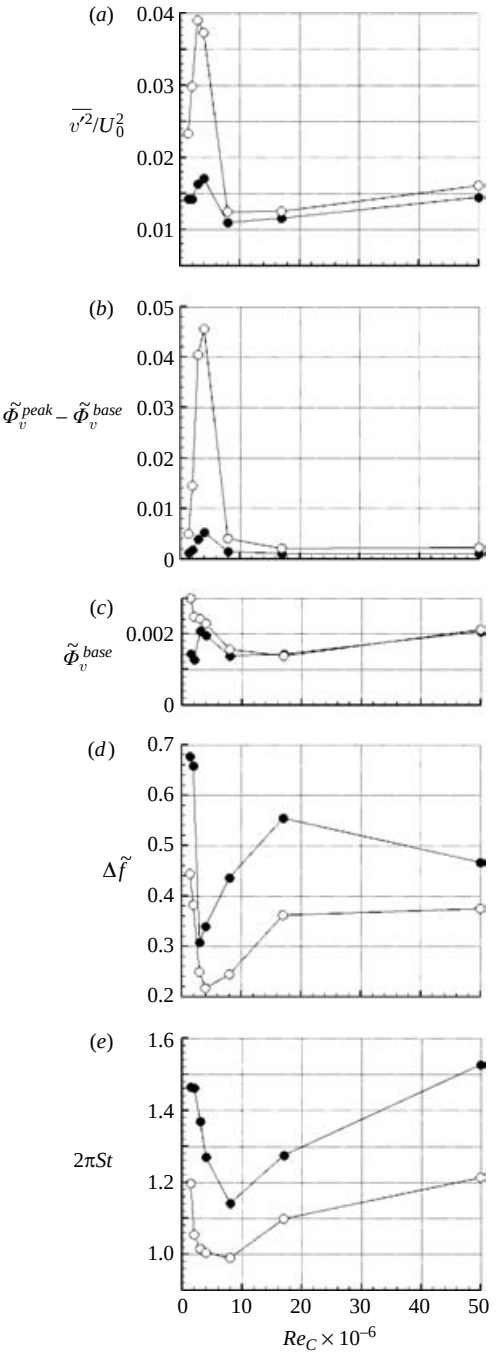

FIGURE 14. Characteristics of LDV-measured vertical-velocity near-wake spectral peaks at $x/C = 1.01$ *vs.* Re_C in millions: Geometry I —●—, and Geometry II —○—. Parameters are illustrated in figure 16. (*b*) The normalized vertical velocity variance, the height of the spectral peaks above the spectral background. (*c*) The spectral background value. (*d*) The spectral peak width. (*e*) The frequency of the spectral peak presented as a *St* multiplied by 2π.

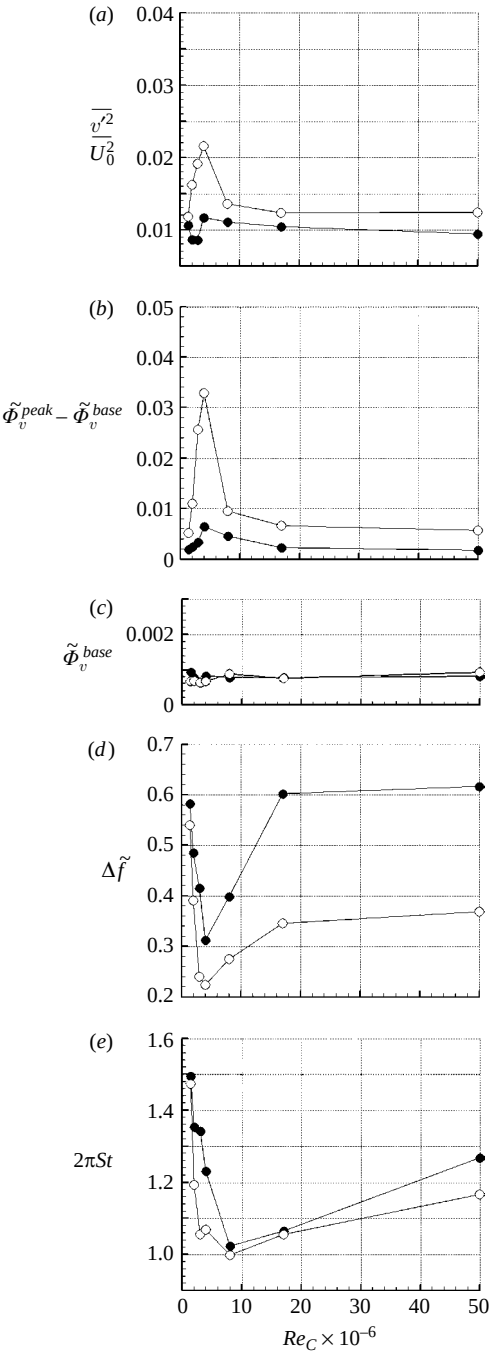

FIGURE 15. Same as figure 20 except these data are from $x/C = 1.07$.

The trends found in the vertical velocity spectra were confirmed by temporal surface-pressure fluctuation spectra, $\boldsymbol{\Phi}_p(f)$, measured on the pressure side of the foil at $x/C = 0.99$ for both trailing edges (see figure 17). These spectra are normalized in a manner similar to the velocity spectra: $\overline{p'^2}/Q_o^2 \equiv (\Delta_y^{nom}/U_0)\int_{-\infty}^{+\infty} \tilde{\boldsymbol{\Phi}}_p \, \mathrm{d}f$, where

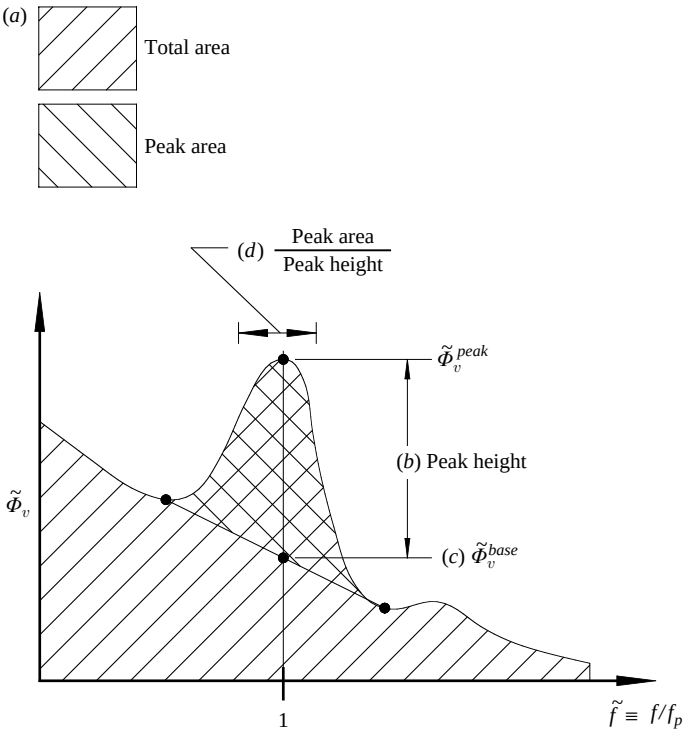

FIGURE 16. Illustration of the parameters used to quantify the LDV-measured vertical velocity spectral peaks in the near wake. Letters correspond to the parts in figures 14 and 15.

$\tilde{\boldsymbol{\Phi}}_p$ is the normalized spectrum, $Q_o \equiv \rho U_0^2/2$, and ρ is the density of water at 32 °C. Here, $\overline{p'^2}/Q_o^2$ is less than 10^{-4} for $Re_C > 3$M for both trailing edges. The upward translation of the curves in figure 17 as Re_C falls below 8M reflects the increasing spectral contribution from noise that does not scale with Q_o^2. Pressure fluctuation data below $Re_C = 3$M are dominated by noise and are not presented. The diagonal lines below the spectra in figure 17 have a slope of -1.

Two fluid dynamic phenomena are evident in the plotted pressure spectra. First, the measured surface pressure fluctuations are generally broadband with a shallow spectral slope, a finding consistent with spectral results for attached turbulent boundary layers (see Willmarth 1975; Farabee & Caserella 1991; Goody 2002). Secondly, spectral pressure fluctuation peaks occur at the anticipated vortex-shedding frequency for Geometry II (figure 17*b*). The pressure spectra for Geometry I (figure 17*a*) are presumed to lack significant peaks because the weaker vortex shedding for this geometry did not produce trailing-edge pressure fluctuations that rose above the turbulent boundary-layer fluctuations. Aside from this discrepancy, the surface pressure fluctuation spectra and the velocity spectra are consistent, and together suggest that vortex shedding is present in the foil's near wake under certain conditions, with $Re_C = 4$M and Geometry II providing the strongest shedding.

To further confirm this interpretation of the spectral results, the spatial PIV measurements were used to visually assess the vortical organization of the foil's near wake. Although this is commonly accomplished by analysing the vorticity component, ω_z, perpendicular to the PIV measurement plane, identification of individual vortices within a flow having mean shear may be enhanced by analysing *swirling strength*,

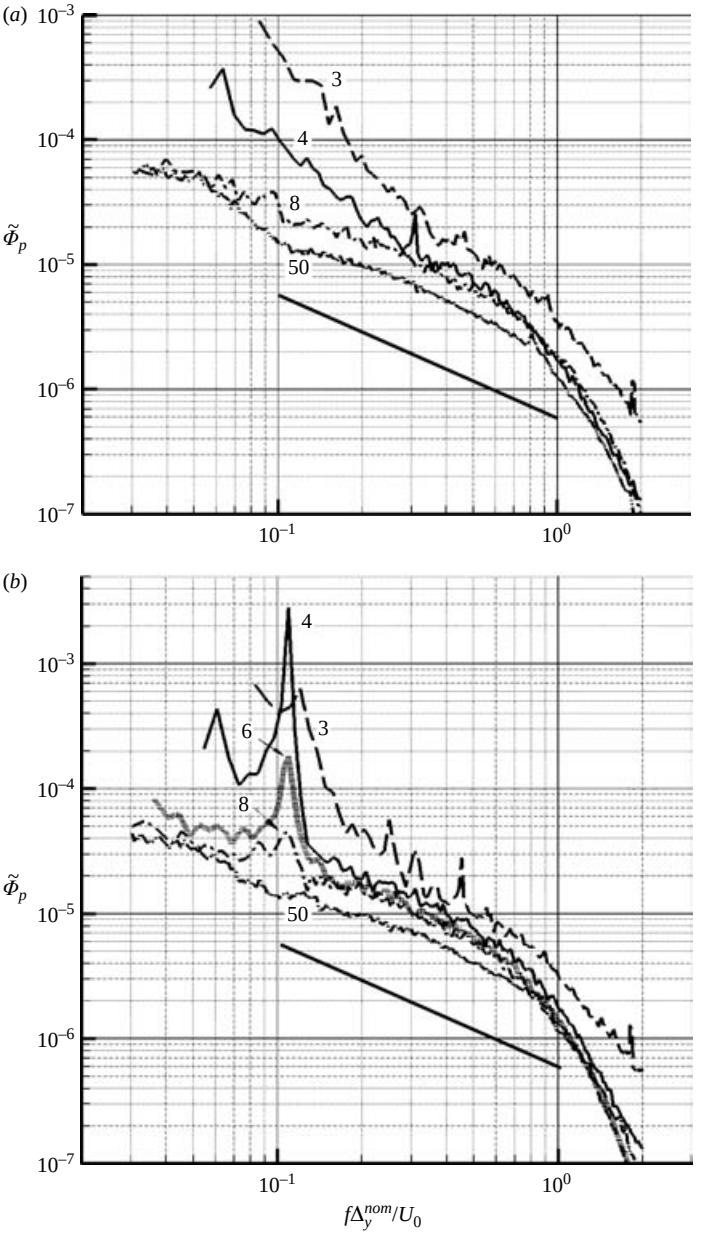

FIGURE 17. The power spectra of the pressure-side surface pressure fluctuations at $x/C = 0.99$ at various Re_C for (*a*) Geometry I and (*b*) Geometry II. Numerals indicate Re_C in millions. The solid line below the data has a slope of -1.

the absolute value of the imaginary part of the eigenvalues of the two-dimensional velocity gradient tensor (Zhou *et al.* 1996, 1999; Adrian, Christensen & Liu 2000). For comparison, ω_z is the difference of off-diagonal terms of the same tensor while swirling strength, χ (with units of inverse time like vorticity), specifies the orbital rotation rate of a fluid element centred on the point of interest. However, χ is zero in pure shear flow (for example when $\partial u/\partial y \neq 0$ and $\partial v/\partial x = 0$), and thus is capable

of indicating where $\partial u/\partial y$ and $\partial v/\partial x$ contribute commensurately to the vorticity in the PIV measurements of the foil's near-wake flow. This is important for vortex identification in regions where the average ω_z of the separated boundary layers is high ($x/C < 1.03$). Thus, χ was chosen in lieu of ω_z to identify vortices, and, in the current discussion, regions of high χ are referred to as vortices.

Figure 18 shows five selected instantaneous swirling strength fields for Geometry I at $Re_C = 4\text{M}$ and for Geometry II at $Re_C = 1.4\text{M}$, 4M, 17M and 50M. Here, clockwise rotating fluid appears white and counterclockwise rotating fluid appears black. The requisite velocity derivatives were computed on a 1.6 mm grid from a central difference stencil of width 3.2 mm. In addition, the computed swirling strength was spatially smoothed with a boxcar filter of 3.2 mm × 3.2 mm, thresholded to remove low-level values, and plotted with the median grey level set to maximize contrast. These manipulations set the minimum size of the visualized vortices.

The fields shown on figure 18 best illustrate the prevailing differences found across all test conditions. The lone field shown for Geometry I (figure 18*a*) is similar in appearance to all results with this trailing edge. The four fields shown for Geometry II illustrate the variability in the extent of near-wake vortex organization found at different Re_C. The vortex-shedding frequency is apparent in the spacing of the largest pressure-side (black) vortices. For example, the streamwise spacing of the vortices at $x/C = 1.045$ and $x/C = 1.10$ in figure 18(*c*) is approximately $5.5\Delta_y^{nom}$, which matches the expected St value of $1/2\pi$ provided the local convection velocity in the foil's near wake is 10 % to 15 % slower than U_0. In addition, the presence of four pressure-side vortex concentrations in figure 18(*b*) compared to three such concentrations in figure 18(*c*) is consistent with the higher St found at the lower Re_C (see figures 13*b* and 15*e*). Furthermore, at $Re_C = 17\text{M}$ and 50M, figures 18(*d*) and 18(*e*), the visual coherence of the swirling strength field is reduced, and this is consistent with the lower spectral peaks measured at these Re_C.

To further assess the spatial organization of the foil's near-wake vortices, the swirling strength fields derived from the PIV measurements were conditionally averaged based on the presence or absence of a pressure-side vortex near $x/C = 1.05$. First, fields lacking a pressure-side vortex within a spatial window of $1.045 < x/C < 1.055$ were discarded, leaving typically half of the original field measurements. Next, the remaining fields were shifted horizontally so that the pressure-side vortex of greatest peak vorticity within the selection window was centred on $x/C = 1.050$ (the selection window is far enough downstream so that either vorticity or swirling strength may be used to identify the strongest vortex within the window). Then, the shifted fields were ensemble averaged. This conditional averaging technique, which mimics conventional phase averaging, is based on pressure-side vortex identification alone, so any suction-side vortex structure that emerges from the averaging is genuinely indicative of vortex street organization.

The results of this conditional averaging are shown in figure 19 for the same panel arrangement and flow conditions as figure 18. The central black feature in each part is the average pressure-side vortex near $x/C = 1.05$. The other Geometry I results are similar to figure 19(*a*). A comparison of figure 19(*b*) to 19(*e*) for Geometry II shows that $Re_C = 4\text{M}$ produces the most organized vortex wake. The pressure-side vortices at $Re_C = 1.4\text{M}$ (figure 19*b*) are almost as organized as those at $Re_C = 4\text{M}$, but the suction-side vortices are spatially less coherent at the lower Re_C. Results at both of the higher Re_C (figures 19*d* and 19*e*) indicate little spatial coherence between pressure- and suction-side vortices. These conditionally averaged results confirm the prior interpretations of the foil wake's relative organization drawn from spectra and

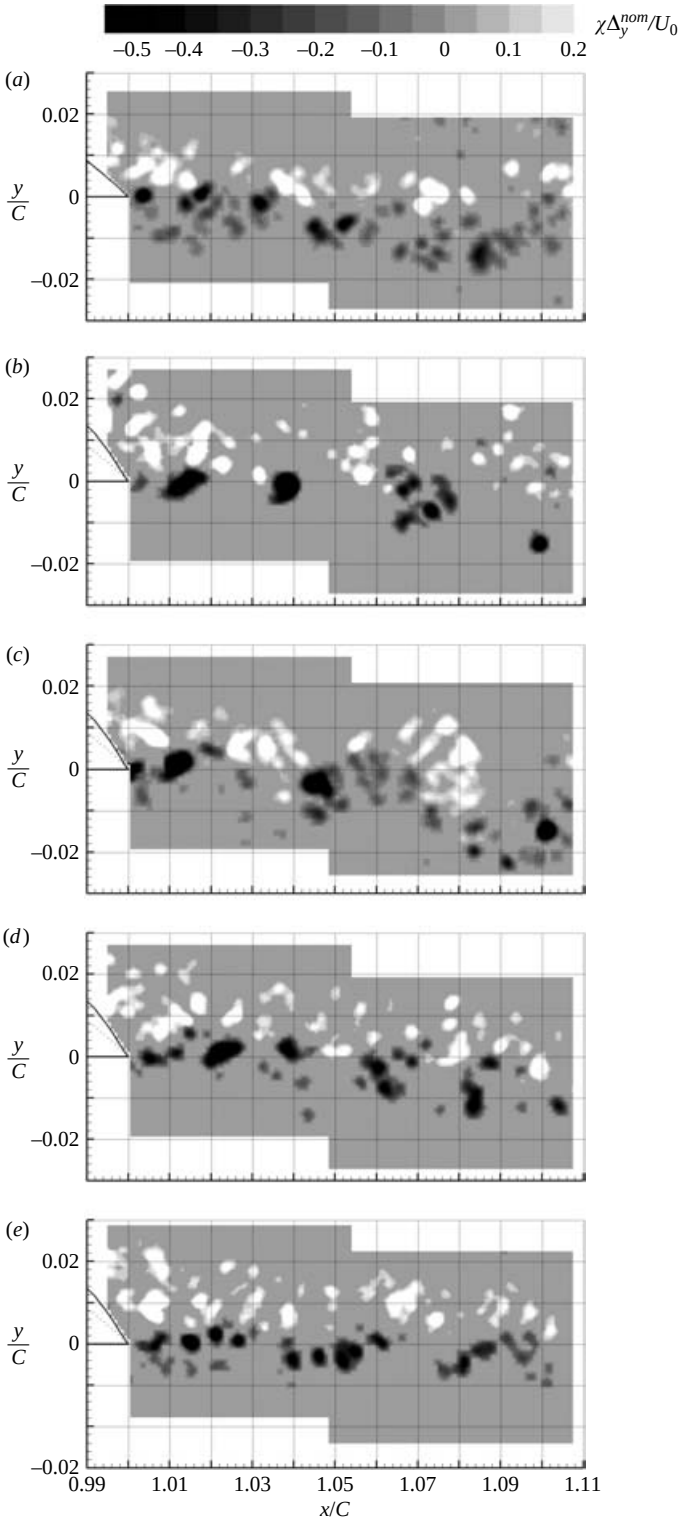

FIGURE 18. Instantaneous PIV fields of normalized swirling strength, $\chi\Delta_y^{nom}/U_0$ for (*a*) Geometry I at $Re_C = 4$M, and Geometry II at (*b*) $Re_C = 1.4$M, (*c*) 4M, (*d*) 17M, (*e*) 50M.

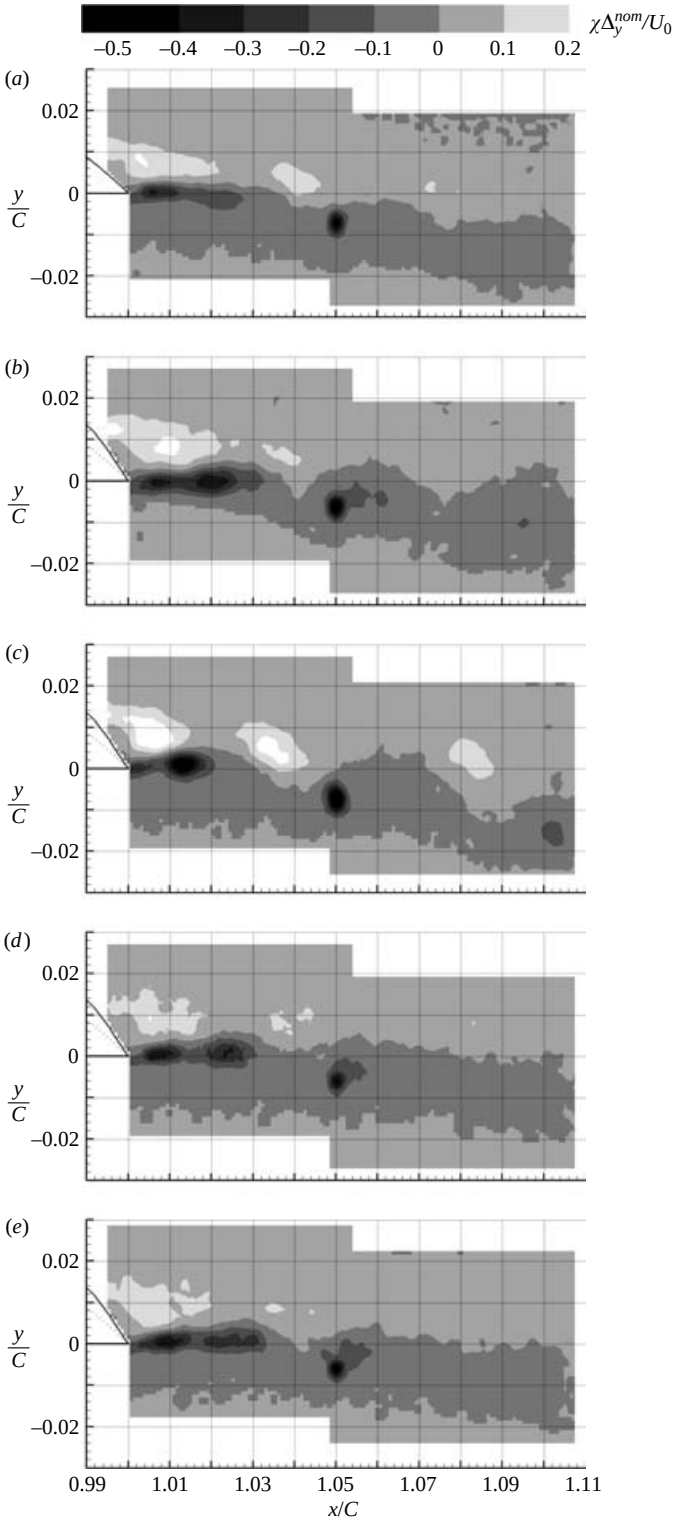

FIGURE 19. Conditionally-averaged PIV fields of normalized mean swirling strength, $\chi\Delta_y^{nom}/U_0$, rendered as greyscale images. The parts follow the same arrangement as figure 18.

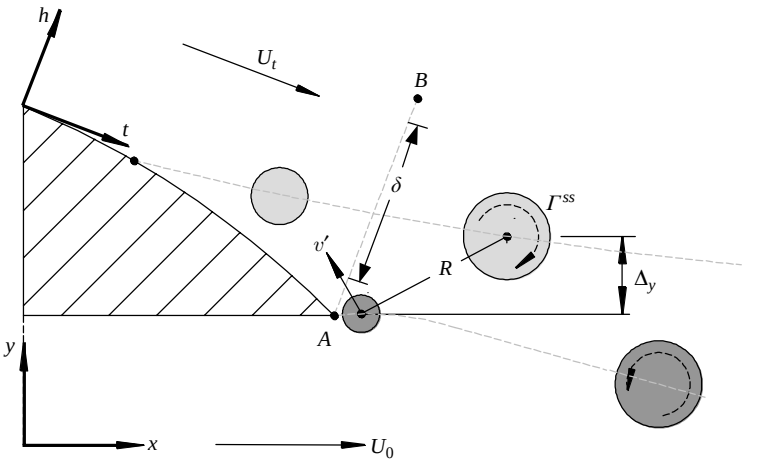

FIGURE 20. Flow cartoon leading to a scaling law for the velocity fluctuation induced at the foil's trailing edge by a suction-side vortex. The size of the induced velocity at the trailing edge is assumed to set the strength of the shed vortex. The suction-side vortex strength is estimated from the flux of vorticity across surface A–B.

the instantaneous fields. In particular, the Geometry II $Re_C = 4\text{M}$ results shown in figure 19(*c*) indicate that near-wake vortex structure extends throughout the PIV measurement domain, and this is consistent with this flow condition producing the narrowest and strongest spectral peaks (see figures 13 to 15 and 17). Additional analyses of the swirling strength fields are provided in Bourgoyne (2003).

4. Scaling of vortex-shedding strength

As is clear from the present and prior results, the combined influences of trailing-edge geometry and boundary-layer characteristics – here varied by changing *Re* – determine the relative strength and spatial organization of near-wake vortices. The goal of this section is to present a simple scaling law for vortex-shedding strength drawn from a heuristic flow cartoon involving suction- and pressure-side vortices in the foil's near wake. This scaling law might be useful for predicting the existence of vortex shedding in flows where only time-averaged measurements or mean-flow predictions are available.

The vortex-shedding scaling law is based on a postulated link between the Biot-Savart induced velocity fluctuations at the foil's trailing edge and the roll-up of the pressure-side shear layer into vortices. Consider the idealized vortex arrangement depicted in figure 20. The suction-side flow is best described in approximate streamline coordinates in which the flow-tangent t-direction and the flow-perpendicular h-direction are parallel and normal to the foil's suction-side surface at $x/C = 0.93$. Here, it is proposed that vortex shedding is significantly enhanced by the imposition of a velocity fluctuation, v', which acts at the trailing-edge apex to initiate the roll-up of the pressure-side shear layer. As the flow evolves beyond the instant shown in figure 20, the velocity ratio v'/U_0 sets the input perturbation level to the Kelvin–Helmholtz instability of the pressure-side shear layer. Such instabilities have been found to be active in other separated turbulent flows (Song & Eaton 2002) and the proposed role of v'/U_0 at the trailing edge is consistent with the established characteristics of vortex shedding. For example, trailing-edge motion that increases the vertical component

of v'/U_0 has been shown to enhance vortex shedding and decrease the vortex street formation length in wind-tunnel tests of a strut with a bevelled trailing edge at $Re_C \sim 1$M (Greenway & Wood 1973). In addition, the use of splitter plates (Roshko 1955l; Morkovin 1964; Bearman 1965) and base bleed (Bearman 1967; Wood 1967) are known to reduce vortex shedding, and modification of v'/U_0 at the trailing edge may be the mechanism behind these effects. Finally, Kuethe (1972) showed for both a flat plate and a lifting surface at Re_C approaching 1M, that the diversion of a portion of the boundary-layer vorticity into streamwise vortices (by a wavelike static surface feature) suppressed vortex street development in the near wake. Such streamwise vortices may disrupt vortex shedding by destroying spanwise coherence of v'/U_0 at the trailing edge. Thus, the strength and spatial correlation of large near-wake vortices formed at the shedding frequency should increase when v'/U_0 increases.

The vortices primarily responsible for v' at the trailing edge are presumed to come from the suction side of the foil because these vortices will be closest to the trailing edge when the next pressure-side vortex is beginning to form. If the near-wake flow is at least locally two-dimensional, the magnitude of v' can be estimated from the geometry in figure 20:

$$\frac{v'}{U_0} \approx \frac{\Gamma^{ss}}{2\pi R U_0}, \tag{1}$$

where Γ^{ss} is the circulation of the suction-side vortex and R is its distance from the trailing edge. The circulation of the suction-side vortex can be estimated from the integrated amount of vorticity that passes the trailing edge in one flow oscillation,

$$\Gamma^{ss} \approx (\mathrm{d}U_t/\mathrm{d}h)^{ss}\delta U_0/f_p. \tag{2}$$

Here, $(\mathrm{d}U_t/\mathrm{d}h)^{ss}$ is a representative suction-side vorticity or shear rate, δ is the thickness of the suction-side shear layer, f_p is the vortex-shedding frequency, and U_0 is used as an estimate of the vortex convection velocity U_t. Combining (1) and (2), taking $\delta \sim R$, approximating St as a constant, and dropping the 2π produces:

$$\frac{v'}{U_0} \propto \frac{(\mathrm{d}U_t/\mathrm{d}h)^{ss}}{f_p} = \frac{1}{St}\frac{(\mathrm{d}U_t/\mathrm{d}h)^{ss}}{U_0/\Delta_y} \propto \frac{(\mathrm{d}U_t/\mathrm{d}h)^{ss}}{U_0/\Delta_y}, \tag{3}$$

where $St = f_p\Delta_y/U_0$ and Δ_y is the near-wake thickness. Consequently, if the relative strength of near-wake vortex shedding is set by v'/U_0 at the foil's trailing edge, then vortex-shedding strength results should collapse when plotted against the dimensionless shear rate at the right of (3), a parameter that can be calculated from trailing-edge mean-flow profiles (i.e. figure 18 of Bourgoyne *et al.* 2003). Here, $(\mathrm{d}U_t/\mathrm{d}h)^{ss}$ was calculated as the average velocity gradient from 3.2 mm below to 3.2 mm above the streamwise velocity-fluctuation peak along a line that intersects the foil's trailing edge and is perpendicular to the local flow direction (line A–B on figure 20).

The form of the right-hand side of (3) is similar to the shedding-strength parameter b/δ^*suggested in Blake (1986), where b is the vertical thickness of the body and δ^* is the average of the suction- and pressure-side boundary-layer displacement thicknesses. Based on a review of experimental data up through the early 1980s, strong vortex shedding was found to occur when $b/\delta^* \geqslant 0.3$ for turbulent flow airfoils (Re_C near or above approximately 2M). The proposed parameter is a refinement of these ideas.

Figure 21 shows the vortex-shedding results from this investigation at $x/C = 1.01$, drawn from figure 14 and from the prior wind-tunnel investigations of Blake (1984) for struts with asymmetric trailing edges using the scaling suggested by (3). Results from Geometry I and II are shown as black and open circles, respectively, with one

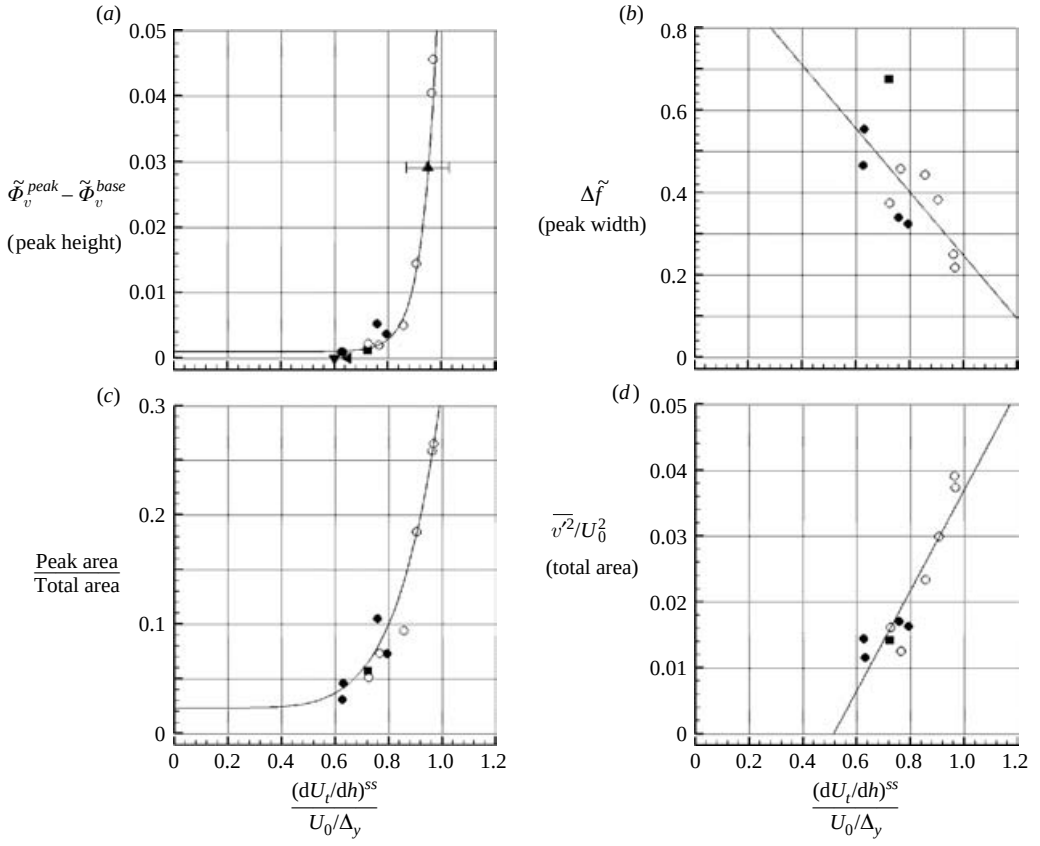

FIGURE 21. Vortex-shedding characteristics for the trailing-edge flows of this study and for a minimally lifting strut (Blake 1984) *vs.* the dimensionless shear rate parameter, $(dU_t/dh)^{ss}/(U_0/\Delta_y)$. Shedding parameters ($y$-axes) are extracted from the LDV temporal spectra at $x/C = 1.01$ (see figures 16, 19 and 20). The mean suction-side shear rate, from Bourgoyne (2003) figure 28, p. 152, is scaled by the measured wake thickness, Δ_y, given in the text to form the x-axes in this figure. The grey triangles indicate strut data: strut with 45° rounded trailing edge ▲; 25° rounded trailing edge ▼; and strut with 25° sharp trailing edge ◄. The solid lines indicate curve fits (*a*) $y = 0.001 + 10^{-9}\,e^{18x}$, (*b*) $y = 1.02 - 0.77x$, (*c*) $y = 0.023 + 0.29x^6$, and (*d*) $y = -0.039 + 0.076x$.

exception. datum on each panel from Geometry I at $Re_C = 1.4$M is depicted as a black square to indicate the unique occurrence of pressure-side boundary-layer separation upstream of the trailing edge at this flow condition. Here, the wake thickness Δ_y is the measured vertical distance between the suction-side Reynolds stress peak at $x/C = 1.009$ and the pressure-side Reynolds stress peak at $x/C = 1.002$. Using this definition, the wake thicknesses for Geometry I are $0.0085C$ at $Re_C = 3$M, $0.0080C$ at $Re_C = 4$M, and $0.0090C$ at the remaining Re_C. The wake thickness for Geometry II is $0.0095C$ at all Re_C. The three grey triangles in figure 21(*a*) are the prior wind-tunnel results of Blake. The error bars for two of these data points at the bottom of figure 21(*a*) are omitted for graphical clarity, but are similar to that shown for the third point. The curves and lines within the four panels of figure 21 are merely simple empirical fits to the data.

Most significantly, figure 21(*a*) shows that the vertical velocity spectral peak height (a convenient measure of vortex-shedding strength) collapses well with the proposed

scaling. The rapid increase in the shedding strength as the dimensionless shear rate approaches unity is due both to an increase in vortex strength and to a reduction in the vortex formation distance. Differences in trailing-edge geometry are accounted for in the scaling through Δ_y that tends to be larger for the blunter Geometry II that places the suction- and pressure-side boundary-layer separation points vertically farther apart than for the more slender Geometry I. Differences in suction-side boundary-layer properties are accounted for in the scaling through $(\mathrm{d}U_t/\mathrm{d}h)^{ss}$ which tends to be larger for Geometry II because the suction-side boundary layer at separation is not as diffused as it is for Geometry I. The spectral peak area ratio in figure 21(*c*) and the overall fluctuation level on figure 21(*d*) also collapse well using the proposed scaling. The collapse for the spectral peak width on figure 21(*b*) is not as successful as for the others parameters, but improves if the Geometry I $Re_C = 1.4\mathrm{M}$ datum is excluded. Although successful within the confines of the available experimental data, the simple scaling suggested by (3) has at least one potential limitation; it does not include the characteristics of the pressure-side boundary layer at separation even though trailing-edge vortex shedding might reasonably be expected to depend on the trailing-edge properties of the boundary layers from both sides of the foil. One possible explanation for the success of (3) in this regard is the asymmetry in boundary-layer separation location between the suction and pressure sides of the foil. The foil's suction-side boundary layer separates upstream of the trailing edge while the pressure side boundary layer separates at the trailing edge for $Re_C > 1.4\mathrm{M}$. Hence, the more-fully-formed suction-side vortices may dominate the interaction between the two shear layers in the foil's near wake. A second explanation follows from the lack of variation in the foil's pressure-side shear-layer characteristics in these experiments when compared to variations in the suction-side shear layer; a mild dependence of vortex shedding on pressure-side shear-layer characteristics might be present but undetected within the available experimental data. The only robust pressure-side shear-layer variation observed in these experiments – a thickening caused by pre-trailing-edge boundary-layer separation for Geometry I at $Re_C = 1.4\mathrm{M}$ – merely influences the bandwidth of vortex shedding, not its spectral amplitude (see figure 21). However, the importance of pressure-side shear-layer characteristics is expected to increase for more symmetric foils, or when suction- and pressure-side boundary-layer separation points and initial shear-layer conditions are more similar.

Although not explicitly incorporated in the scaling suggested by (3), near-wake symmetry plays a role in whether or not strong vortex shedding occurs near the foil's trailing edge. When strong vortex shedding is absent, the near-wake shear layers tend to roll up on length scales set by the separating boundary layers (Morris & Foss 2001). Such small-scale roll-up is evident in the flow visualization of Prasad & Williamson (1997) for the wake of a cylinder with vortex shedding at $Re_d = 10^4$ in which the shear layers roll up first on the smaller boundary-layer scale and then further downstream on the larger wake scale. This phenomenon is also evident in the present measurements for Geometry II at $Re_C = 50\mathrm{M}$ where the preferred roll-up frequency in the initial pressure-side shear layer is higher than the expected vortex-shedding Strouhal frequency (note the three groups of four pressure-side vortices in figure 18*e*). Thus, when the suction- and pressure-side shear layers at the trailing edge are different enough to have incommensurate instability frequencies, formation of an organized vortex street may be delayed or even suppressed. Such reasoning also suggests that matched suction- and pressure-side shear layers at the foil's trailing edge should lead to strong near-wake vortex shedding, and this deduction is consistent with the present investigations. The flow condition that produced the most symmetric

trailing-edge shear layers, Geometry II at $Re_C = 4$M, also produced the strongest vortex shedding. Thus, the success of the simple scaling may arise from $(\mathrm{d}U_t/\mathrm{d}h)^{ss}/(U_0/\Delta_y)$ quantifying the extent of symmetry between the more-diffuse suction-side shear layer and the thinner pressure-side shear layer at the foil's trailing edge.

Even with the potential limitation identified above, the success (perhaps fortuitous) of the simple scaling suggested by (3) implies that

$$\frac{(\mathrm{d}U_t/\mathrm{d}h)^{ss}}{U_0/\Delta_y} \geqslant 0.8 \tag{4}$$

can be used to predict when near-wake vortex shedding will occur when boundary conditions, mean-flow calculations or measurements, or other sources of information provide values for $(\mathrm{d}U_t/\mathrm{d}h)^{ss}$, U_0, and Δ_y. The main problem with using (4) for predictions is that $(\mathrm{d}U_t/\mathrm{d}h)^{ss}$ is influenced by the vortex shedding. However, vortex shedding tends to decrease $(\mathrm{d}U_t/\mathrm{d}h)^{ss}$ so (4) is likely to be conservative and will tend to overpredict the presence of vortex shedding from estimates of $(\mathrm{d}U_t/\mathrm{d}h)^{ss}$, U_0, and Δ_y. Further discussion of (4), as well as an alternative form of figure 21 in which the measured *St* is included in the dimensionless shear rate is provided in Bourgoyne (2003).

5. Summary and conclusions

The near-wake fluctuations of a two-dimensional hydrofoil at low Mach number have been experimentally investigated at chord-based Reynolds numbers from 1.4 million to 50 million for two trailing edges having 44° and 56° apex angles. The LDV, PIV and fluctuating surface pressure measurements reported here quantify the phenomenon of near-wake vortex shedding behind a hydrofoil with a compact region of separation and the conditions under which such vortex shedding occurs. In addition, the turbulence statistics reported here form a unique high-Reynolds-number data set when combined with the average flow results in Bourgoyne *et al.* (2003). This effort has lead to four main findings.

(i) The turbulent fluctuations in the foil's near wake are Reynolds-number dependent because of the varying strength of structured near-wake vortex shedding. The observed near-wake variations arise from the subtle *Re*-dependence of the separating suction- and pressure-side boundary layers that interact to form the foil's near wake. The relative strength of the vortex shedding was found to depend on trailing-edge geometry as well, with the thicker or blunter trailing edge producing stronger vortex shedding.

(ii) Strong vortices from both the suction- and pressure-side shear layers are organized into a staggered vortex street that dominates the near-wake fluctuations when vortex shedding occurs. In spite of the asymmetry of the flow past the foil's trailing edge, conditions were not found in which either the suction-side or the pressure-side vortices alone were able to establish a structured arrangement of strong near-wake vortices, although Geometry II at $Re_C = 1.4$M approaches this situation. When vortex shedding is weak or absent, pressure-side vortices dominate the fluctuations in the foil's near wake, but there is little or no prevalent geometrical structure of the wake vortices. The resulting velocity and foil-surface-pressure fluctuations are broadband compared to the vortex-shedding cases.

(iii) Biot-Savart-induced velocity fluctuations at the foil's trailing edge appear to control the strength of near-wake vortex shedding. This finding is consistent with the measured near-wake fluctuations reported here and with prior investigations of vortex shedding involving enhancement and suppression techniques.

(iv) The proposed scaling of vortex-shedding strength based on the mean suction-side vorticity or shear rate, the upstream velocity, and the wake thickness is successful throughout the Re_C parameter range of this study for both trailing-edge geometries. Furthermore, the proposed scaling is consistent with prior studies at lower Reynolds number on struts with asymmetric trailing edges. Although this shedding strength scaling relies on time-averaged flow parameters, it may be possible to use it to conservatively predict when vortex shedding will occur from time-averaged flow properties obtained from computations, measurements, correlations, or other sources. Of course, stability theory potentially offers an alternative means of predicting the likelihood of vortex shedding when the time-averaged flow is known, and a stability investigation is a natural next step toward elucidating the role of the trailing-edge time-averaged flow in vortex shedding.

In conclusion, the experimental results presented here and in Bourgoyne *et al.* (2003) bridge the Reynolds-number gap between prior studies of near-wake vortex shedding and full-scale lifting-surface applications. In addition, they form a unique data set for the development and validation of scaling laws and computational models for high-Reynolds-number turbulence.

The authors wish to the acknowledge the contributions of Shiyao Bian, Joshua Hamel, Carolyn Judge and Kent Pruss of the University of Michigan; William Blake, Michael Cutbirth, Ken Edens, Bob Etter, Ted Farabee, Jon Gershfeld, Joe Gorski, Tom Mathews, David Schwartzenberg, Jim Valentine, Phil Yarnall, Joel Park and the LCC technical staff from the Naval Surface Warfare Center – Carderock Division; and Pat Purtell and Candace Wark from the Office of Naval Research, Code 333, which supported this research under contract numbers N00014-99-1-0341 and N00014-99-1-0856.

REFERENCES

Adrian, R. J., Christensen, K. T. & Liu, Z.-C. 2000 Analysis and interpretation of instantaneous turbulent velocity fields. *Exps. Fluids* **29**, 275–290.

Bearman, P. W. 1965 Investigation of the flow behind a two-dimensional model with a blunt trailing edge fitted with splitter plates. *J. Fluid Mech.* **21**, 241–255.

Bearman, P. W. 1967 The effect of base bleed on the flow behind a two-dimensional model with a blunt trailing edge. *Aero. Q.*, August.

Blake, W. K. 1975 A statistical description of the pressure and velocity fields at the trailing edges of flat struts. *Rep. 4241*, David Taylor Naval Ship Research and Development Center, Bethesda, MD.

Blake, W. K. 1984 Trailing edge flow and aerodynamic sound, Parts 1 and 2. *Rep. DTNSRDC-83/113*, David Taylor Naval Ship Research and Development Center, Bethesda, MD.

Blake, W. K. 1986 *Mechanics of Flow Induced Sound and Vibration*, vol. 2, chap. 11. Academic.

Blake, W. K. & Gershfeld, J. L. 1989 Aeroacoustics of trailing edges. In *Frontiers in Fluid Mechanics* (ed. M. Gad-el-Hak), pp. 457–532. Springer.

Boldman, D. R., Brinich, P. F. & Goldstein, M. E. 1976 Vortex shedding from a blunt trailing edge with equal and unequal mean velocities. *J. Fluid Mech.* **75**, 721–735.

Bourgoyne, D. A. 2003 Flow over a hydrofoil with trailing edge vortex shedding at high Reynolds number. PhD thesis (University of Michigan, Ann Arbor, MI).

Bourgoyne, D. A., Hamel, J. A., Ceccio, S. L. & Dowling, D. R. 2003 Time averaged flow over a hydrofoil at high Reynolds number. *J. Fluid Mech.* **496**, 365–404.

Cicatelli, G. & Sieverding, C. H. 1995 A review of the research on unsteady turbine blade wake characteristics. *AGARD PEP 85th Symp. on Loss Mechanisms and Unsteady Flows in Turbomachines, Derby, UK, May 8–12.*

Cicatelli, G. & Sieverding, C. H. 1996 The effect of vortex shedding on the unsteady pressure distribution around the trailing edge of a turbine blade. *ASME Paper* 96-GT-39.

Farabee, T. M. & Caserella, M. J. 1991 Spectral features of wall pressure fluctuations beneath turbulent boundary layers. *Phys. Fluids* A **3**, 2410–2420.

Gerrard, J. H. 1966 The mechanics of the formation region of vortices behind bluff bodies. *J. Fluid Mech.* **25**, 401–413.

Goody, M. 2002 An empirical spectral model for surface pressure fluctuations that includes Reynolds number effects. *AIAA Paper* 2002-2565.

Greenway, M. E. & Wood, C. J. 1975 The effect of a bevelled trailing edge on vortex shedding and vibration. *J. Fluid Mech.* **61**, 322–335.

Ho, Y.-H. & Lakshminarayana, B. 1997 Computation of unsteady flow field over a hydrofoil, including boundary layer and wake. *AIAA J.* **35**, 40–50.

Howe, M. S. 1999 Trailing edge noise at low Mach numbers. *J. Sound Vib.* **225**, 211–238.

Howe, M. S. 2000 Trailing edge noise at low Mach numbers part 2: attached and separated edge flows. *J. Sound Vib.* **234**, 761–765.

Huerre, P. & Monkewitz, P. A. 1990 Local and global instabilities in spatially developing flows. *Annu. Rev. Fluid Mech.* **22**, 473–538.

Knight, C. J. & Peltier, L. J. 1997 2-D steady wake predictions for airfoil cascades with beveled trailing edges. *AIAA Paper 97-0077*.

Kuethe, A. M. 1972 Effect of streamwise vortices on wake properties associated with sound generation. *J. Aircraft* **9**, 715–719.

Lotfy, A. & Rockwell, D. 1993 The near-wake of an oscillating trailing edge: mechanisms of periodic and aperiodic response. *J. Fluid Mech.* **251**, 173–201.

Lurie, E. A., Keenan, D. P. & Kerwin, J. E. 1998 Experimental study of an unsteady separating boundary layer. *AIAA J.* **36**, 565–570.

Manoha, E., Troff, B. & Sagaut, P. 2000 Trailing-edge noise prediction using large-eddy simulation and acoustic analogy. *AIAA J.* **38**, 575–583.

Minniti, R. J. & Mueller, T. J. 1998 Experimental investigation of unsteady aerodynamics and aeroacoustics of a thin airfoil. *AIAA J.* **36**, 1149–1156.

Morkovin, M. V. 1964 Aerodynamic loads on bluff bodies at low speeds. *AIAA J.* **2**, 11.

Morris, S. C. & Foss, J. 2001 Turbulent boundary layer to single stream shear layer. *Bull. Am. Phys. Soc.* **46**, 134.

Oertel, H., Jr 1990 Wakes behind blunt bodies. *Annu. Rev. Fluid Mech.* **22**, 539–564.

Prasad, A. & Williamson, H. K. 1997 The instability of the shear layer separating from a bluff body. *J. Fluid Mech.* **333**, 375–402.

Roger, M. & Moreau, S. 2002 Trailing edge noise measurements and predictions for subsonic loaded fan blades. *8th AIAA/CEAS Aeroacoustics Conference and Exhibit, 17–19 June, Breckenridge, CO. AIAA Paper 2002-2460.*

Roshko, A. 1955 On the wake and drag of bluff bodies. *J. Aero. Sci.* **22**, 124–132.

Rowe, A., Fry, A. L. A. & Motallebi, F. 2001 Influence of boundary layer thickness on base pressure and vortex shedding frequency. *AIAA J.* **39**(4), Tech. Notes.

Sieverding, C. H. & Heinemann, H. 1990 The influence of boundary layer state on vortex shedding from flat plates and turbine cascades. *J. Turbomach.* **112**, 181–187.

Song, S. & Eaton, J. K. 2002 Reynolds number effects on a turbulent boundary layer with separation, reattachement, and recovery. *Rep.* TSD-146, Mech. Engng Dept. Stanford University, Stanford, CA.

Swales, C. & Lowson, M. V. 1997 Aero-acoustic study on a NACA 0012 airfoil. *AIAA Paper 97-0509*.

Ubaldi, M. & Zunino, P. 2000 An experimental study of the unsteady characterisitics of the turbulent near wake of a turbine blade. *Expl Therm. Fluid Sci.* **23**, 23–33.

Ubaldi, M., Zunino, P., Campora, U. & Ghiglione, A. 1996 Detailed velocity and turbulence measurements of the profile boundary layer in a large scale turbine cascade. *ASME International Gas Turbine & Aerospace Congress and Exposition, Birmingham, UK, Paper 96-GT-42.*

Vetterling, W. T., Teukolsky, S. A., Press, W. H. & Flannery, B. P. 1992 In *Numerical Recipes in C*, 2nd edn. Cambridge University Press.

Wang, M. & Moin, P. 2000 Computation of trailing-edge flow and noise using large-eddy simulation. *AIAA J.* **38**, 2201–2209.

Wang, M. & Moin, P. 2002 Dynamic wall modeling for large-eddy simulation of complex turbulent flows. *Phys. Fluids* **14**, 2043–2051.

Willmarth, W. W. 1975 Pressure fluctuations beneath turbulent boundary layers. *Annu. Rev. Fluid Mech.* **7**, 13–38.

Wood, C. J. 1967 Visualization of an incompressible wake with base bleed. *J. Fluid Mech.* **29**, 259–272.

Wygnanski, I., Champagne, F. & Marasli, B. 1986 On the large scale structures in two-dimensional small-deficit, turbulent wakes. *J. Fluid Mech.* **168**, 31–71.

Zhou, J., Adrian, R. J. & Balachandar, S. 1996 Autogeneration of near wall vortical structures in channel flow. *Phys. Fluids* **8**, 288–290.

Zhou, J., Adrian, R. J., Balachandar, S. & Kendall, T. M. 1999 Mechanisms for generating coherent packets of hairpin vortices in channel flow. *J. Fluid Mech.* **387**, 353–359.